Article

Cell Chemical Biology

Acriflavine, a clinically approved drug, inhibits SARS-CoV-2 and other betacoronaviruses

Graphical abstract

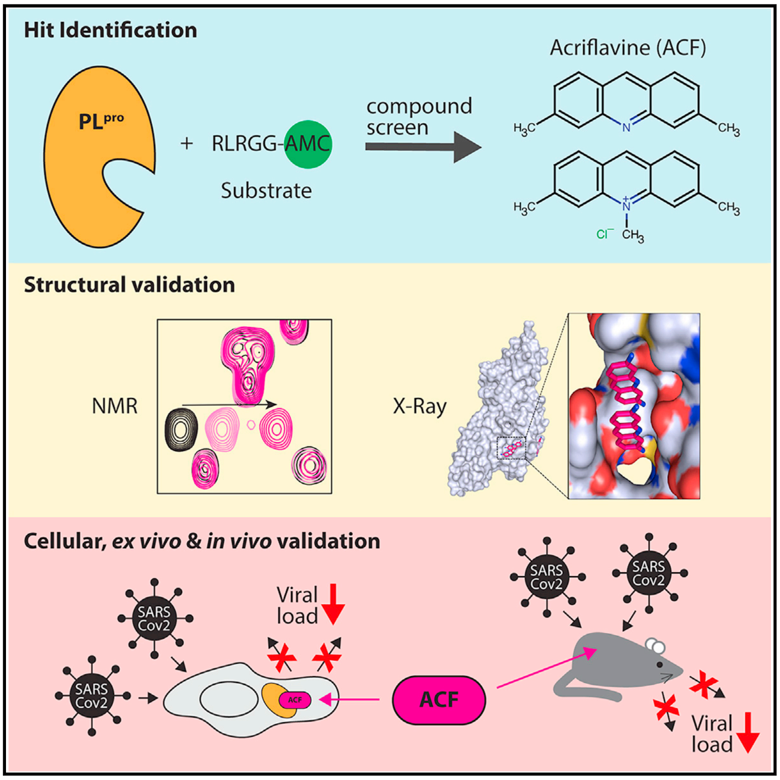

Highlights

- Acriflavine (ACF) is a potent inhibitor of SARS-CoV-2 papain-like protease PL^{pro}
- A co-crystal structure shows how ACF blocks the active site with a unique binding mode
- ACF has low-nanomolar IC_{50} *in vitro*, *ex vivo*, and in animal models
- ACF is a registered drug and a promising candidate for clinical studies

Authors

Valeria Napolitano,
Agnieszka Dabrowska,
Kenji Schorpp, ..., Kamyar Hadian,
Grzegorz Maria Popowicz,
Krzysztof Pyrc

Correspondence

sattler@helmholtz-muenchen.de (M.S.),
kamyar.hadian@helmholtz-muenchen.de (K.H.),
grzegorz.popowicz@helmholtz-muenchen.de (G.M.P.),
k.a.pyrc@uj.edu.pl (K.P.)

In brief

Napolitano et al. discovered acriflavine (ACF), a clinically approved drug, as an effective inhibitor of SARS-CoV-2 papain-like protease (PL^{pro}). ACF inhibits viral replication at nanomolar concentrations *in vitro* and *ex vivo*, as well as *in vivo*. These findings open a promising therapeutic approach against COVID-19 and other betacoronaviruses.

Napolitano et al., 2022, Cell Chemical Biology *29*, 774–784
May 19, 2022 © 2021 The Authors. Published by Elsevier Ltd.
https://doi.org/10.1016/j.chembiol.2021.11.006

CellPress
OPEN ACCESS

Cell Chemical Biology

Article

Acriflavine, a clinically approved drug, inhibits SARS-CoV-2 and other betacoronaviruses

Valeria Napolitano,[3,9] Agnieszka Dabrowska,[1,2,9] Kenji Schorpp,[3,9] André Mourão,[3,9] Emilia Barreto-Duran,[1] Malgorzata Benedyk,[2] Pawel Botwina,[1,2] Stefanie Brandner,[3] Mark Bostock,[3,4] Yuliya Chykunova,[1,2] Anna Czarna,[1] Grzegorz Dubin,[1] Tony Fröhlich,[3] Michael Hölscher,[5] Malwina Jedrysik,[1] Alex Matsuda,[1] Katarzyna Owczarek,[1] Magdalena Pachota,[1,2] Oliver Plettenburg,[3,6,7] Jan Potempa,[2] Ina Rothenaigner,[3] Florian Schlauderer,[3] Klaudia Slysz,[2] Artur Szczepanski,[1,2] Kristin Greve-Isdahl Mohn,[8] Bjorn Blomberg,[8] Michael Sattler,[3,4,10,*] Kamyar Hadian,[3,10,*] Grzegorz Maria Popowicz,[3,4,10,*] and Krzysztof Pyrc[1,10,11,*]

[1]Virogenetics Laboratory of Virology, Malopolska Centre of Biotechnology, Jagiellonian University, Gronostajowa 7a, 30-387 Krakow, Poland
[2]Microbiology Department, Faculty of Biochemistry, Biophysics and Biotechnology, Jagiellonian University, Gronostajowa 7, 30-387 Krakow, Poland
[3]Helmholtz Zentrum München, Ingolstädter Landstrasse 1, 85764 Neuherberg, Germany
[4]Bavarian NMR Center, Department of Chemistry, Technical University of Munich, Lichtenbergstrasse 4, 85748 Garching, Germany
[5]Division of Infectious Diseases and Tropical Medicine, University Hospital, LMU Munich, Leopoldstrasse 5, 80802 Munich, Germany
[6]Centre of Biomolecular Drug Research (BMWZ), Institute of Organic Chemistry, Leibniz Universität Hannover, Hannover, Germany
[7]Institute for Lung Health (ILH), Justus Liebig University, Giessen, Germany
[8]Haukeland University Hospital, Bergen, Norway
[9]The authors contributed equally
[10]Senior author
[11]Lead contact
*Correspondence: sattler@helmholtz-muenchen.de (M.S.), kamyar.hadian@helmholtz-muenchen.de (K.H.), grzegorz.popowicz@helmholtz-muenchen.de (G.M.P.), k.a.pyrc@uj.edu.pl (K.P.)
https://doi.org/10.1016/j.chembiol.2021.11.006

SUMMARY

The COVID-19 pandemic caused by SARS-CoV-2 has been socially and economically devastating. Despite an unprecedented research effort and available vaccines, effective therapeutics are still missing to limit severe disease and mortality. Using high-throughput screening, we identify acriflavine (ACF) as a potent papain-like protease (PL^{pro}) inhibitor. NMR titrations and a co-crystal structure confirm that acriflavine blocks the PL^{pro} catalytic pocket in an unexpected binding mode. We show that the drug inhibits viral replication at nanomolar concentration in cellular models, *in vivo* in mice and *ex vivo* in human airway epithelia, with broad range activity against SARS-CoV-2 and other betacoronaviruses. Considering that acriflavine is an inexpensive drug approved in some countries, it may be immediately tested in clinical trials and play an important role during the current pandemic and future outbreaks.

INTRODUCTION

Coronaviruses have been considered a potential threat since 2002, when the severe acute respiratory syndrome coronavirus (SARS-CoV) emerged in southern China, spreading across continents but disappearing shortly thereafter (Drosten et al., 2003; Ksiazek et al., 2003). Ten years later, Middle East respiratory syndrome coronavirus (MERS-CoV) posed a pandemic threat, but despite high fatality rates, the human-to-human transmission remained limited (Zaki et al., 2012). Despite these warnings, the emergence of the SARS-CoV-2 and the subsequent pandemic found health care largely unprepared and has paralyzed the modern world in an unprecedented way (Iacobucci, 2020; Ma et al., 2020; Mirzaei et al., 2020).

First vaccines are available and applied already, and further approvals are expected shortly (Parker et al., 2020). However, the time needed for vaccination of the global population, limited availability of vaccines, reluctance to vaccinate, and reduced effectiveness of vaccination against newly emerging variants highlight the urgent need for effective antivirals (Saha et al., 2020). The timeline of preclinical to clinical development of novel antivirals, however, is too long for completely new compounds to make a clinical impact during the current pandemic. Repurposing existing drugs with known safety profiles is, therefore, the most efficient and promising option. Initial candidates, unfortunately, did not fulfill expectations (Cao et al., 2020; Horby et al., 2020). Some other leads are still being tested in the clinic, but no convincing proof of efficacy has been provided as yet (Pan et al., 2020; Simonovich et al., 2020). Importantly, it has been proposed that the identification of a set of antivirals against SARS-CoV-2 may provide an opportunity to mimic the strategy effective for HIV-1: combinatorial treatment against different molecular targets (Lu et al., 2018).

The coronaviral genome encodes several structural and nonstructural proteins (Knipe and Howley, 2013), including two

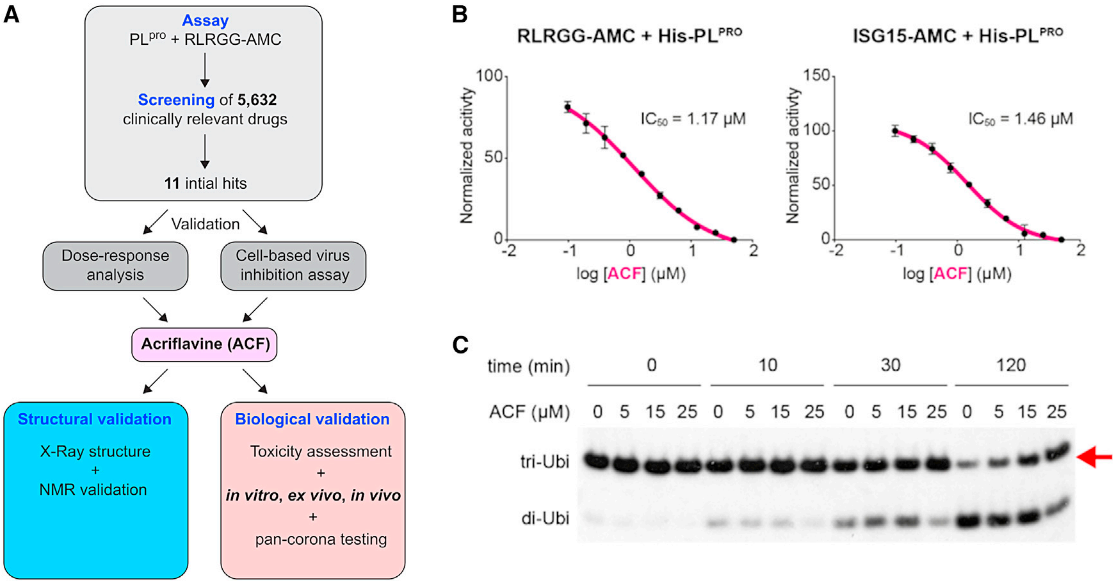

Figure 1. Identification of PL^{pro} inhibitors: ACF as a confirmed hit

(A) General scheme of the study.

(B) Enzymatic activity inhibition assay using RLRGG-AMC (left) or ISG15-AMC (right) as substrates for PL^{pro} performed in technical triplicates. The vertical axis shows the relative enzyme activity as a function of ACF concentration.

(C) Time course analysis of tri-ubiquitin K48-linked (2 μM) hydrolysis using 100 nM PL^{pro} in the presence of different ACF concentrations. Red arrow indicates the PL^{pro} substrate.

cysteine proteases, M^{pro} (nsp5) and PL^{pro} (nsp3), essential for the virus's replication (Shamsi et al., 2021). Although extensive actions to identify inhibitors of M^{pro} have been undertaken (Capasso et al., 2020), only scarce information is available for the PL^{pro}. The latter protease is essential for viral protein maturation and has also been attributed other functions, including type I interferon response attenuation, making it a viable therapeutic target (Shin et al., 2020).

Here, we have discovered acriflavine (ACF) as an effective inhibitor of SARS-CoV-2. ACF is a mixture of trypaflavines (3,6-diamino-10-methylacridinium chloride and 3,6-diamino-3-methylacridinium chloride) and proflavine (3,6-diaminoacridine). ACF has been used systemically against sleeping sickness, urinary tract infections, and gonorrhea and has been suggested to be effective for a number of other indications (Dana et al., 2014; Funatsuki et al., 1997; Kawai and Yamagishi, 2009; Manchester et al., 2013; Mathé, 2000; Pépin et al., 2017; Persinoti et al., 2014; Tripathi et al., 2006). ACF was tested in a clinical trial against HIV where up to 100 mg daily was administered over the course of several months. Despite the chemical structure suggesting possible DNA intercalation and liver toxicity, no adverse effects were observed in these studies (Mathé et al., 1996, 1998). ACF has been approved in the past and has been present in European pharmacopeias for systemic use (Browning, 1943, 1967; Mathé et al., 1998; Wainwright, 2001). Importantly, in some countries, ACF is currently available as an over-the-counter medicine (e.g., Brazil; EMS Cystex) against urinary tract infections. Its safety and efficacy were tested in a recently completed clinical trial (Gama et al., 2020; NCT03379389, 2020). In other countries, ACF is used as an ingredient in mouthwash advised for children ("Michino" gargle in Japan) (Lee et al., 2009). The extensive available studies on the long-term systemic administration of large doses of ACF have not revealed any major side effects, suggesting that it could be employed alone or in combination with other drugs (Nehme et al., 2020) after completion of clinical trials.

Our data demonstrate that ACF is a potent inhibitor of SARS-CoV-2 PL^{pro}, opening a promising therapeutic approach against COVID-19. The mode of action is confirmed by structural characterization with X-ray crystallography and NMR, demonstrating that ACF specifically inhibits the active site of the enzyme with an unprecedented binding mode. We show that ACF blocks the virus infection *in vitro*. Importantly, the viral infection is also suppressed *ex vivo* in human airway epithelium (HAE) cultures, which recapitulate the fully differentiated human airway epithelium, as well as in an *in vivo* mouse model, where ACF can reach therapeutic levels with good pharmacokinetics upon oral delivery. Finally, we provide evidence for ACF's antiviral effect against other betacoronaviruses, making this a potentially important therapeutic against future pandemics.

RESULTS

Identification and validation of PL^{pro} repurposed inhibitors

ACF was identified in a high-throughput screening approach for inhibitors of PL^{pro}. We established a protease assay using a fluorogenic substrate. The overall scheme of this study is presented in Figure 1A. On the basis of the screening of a library consisting of 5,632 small-molecule compounds, which are either approved or are/have been at various stages of clinical testing (Corsello et al., 2017), we selected 11 compounds for validation

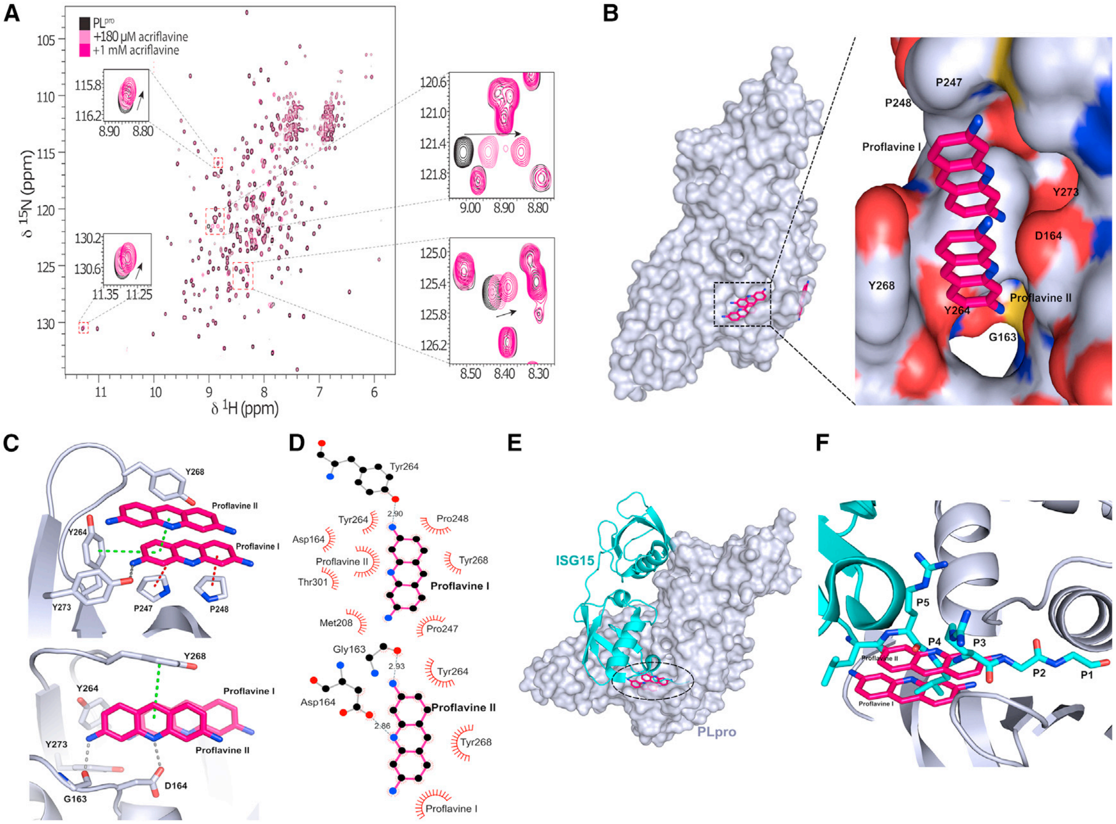

Figure 2. Structural details of PL^{pro} inhibition by proflavine

(A) ^{1}H,^{15}N heteronuclear correlation NMR spectra of ^{15}N-labeled PL^{pro} titrated with ACF indicate a localized binding.

(B) Crystal structure of PL^{pro}-proflavine complex at 2.7 Å. The magnified fragment shows two proflavine molecules inside the substrate-recognition cleft of PL^{pro}.

(C) Intermolecular interaction between PL^{pro} and proflavine molecules. Two π-stacked molecules form a network of hydrogen bonds, π-π interactions, and hydrophobic contacts with PL^{pro}.

(D) Molecular interaction details for the two proflavine molecules.

(E) Overlay of the ISG15-PL^{pro} structure and PL^{pro}-proflavine structure.

(F) A zoomed-in view of the binding pocket reveals that the proflavines are bound in the same site as the C-terminal end of the ISG15 substrate and mimic polar and lipophilic interactions of PL^{pro} with the native substrate.

experiments (Table S1; Figure S1). ACF was the most active compound, with a dose-dependent PL^{pro} inhibition with an IC_{50} of 1.66 μM (Figure 1B). Next, we tested the effect of ACF on PL^{pro} enzymatic activity, using the ISG15-AMC probe as substrate (Klemm et al., 2020; Shin et al., 2020). As shown previously, PL^{pro} cleaves ISG15-AMC significantly faster compared with RLRGG-AMC. Nonetheless, the IC_{50} of ACF with ISG15-AMC (1.46 μM; Figures 1B, S2A, and S2B) was comparable to the IC_{50} determined with the RLRGG-AMC substrate. To eliminate possible fluorescence artifacts, we conducted gel-based de-ubiquitination assays to confirm our results. We incubated K48 tri-ubiquitin with PL^{pro} and took samples at different time points to analyze the cleavage by western blot. PL^{pro} efficiently cleaved K48 tri-ubiquitin to di-ubiquitin (Figures 1C and S2C) as previously shown (Klemm et al., 2020). Next, PL^{pro} was incubated with either DMSO or 5, 15, or 25 μM ACF before K48 tri-ubiquitin chains were added to the reaction mixture. Also in this independent assay format, ACF reduced the protease activity in a dose-dependent manner (Figure 1C), thereby confirming that ACF is a specific PL^{pro} inhibitor.

To evaluate the specificity of ACF, we performed an enzymatic digestion assay using fluorescent M^{pro} substrate. This experiment shows that ACF is a very weak M^{pro} inhibitor, with less than 50% inhibition at 100 μM ACF concentration (Figures S2D and S2E). Therefore, we conclude that M^{pro} inhibition by ACF is not a significant force in reducing SARS-CoV-2 replication.

Structural analysis of SARS-CoV-2 PL^{pro} in complex with proflavine

In order to confirm that ACF binds directly to PL^{pro} in solution, we recorded 2D ^{1}H,^{15}N transverse relaxation-optimized spectroscopy (TROSY) NMR spectra of recombinant ^{15}N-labeled PL^{pro} in the absence and presence of ACF. The spectra of PL^{pro} are consistent with those of a globular folded, monomeric protein in solution (Figure 2A). The addition of ACF induces chemical shift changes for a number of amide signals while not affecting the remaining bulk of the resonances. This confirms that the overall fold and monomeric state of the protein are not affected and demonstrates that ACF binds to a spatially localized site in PL^{pro}.

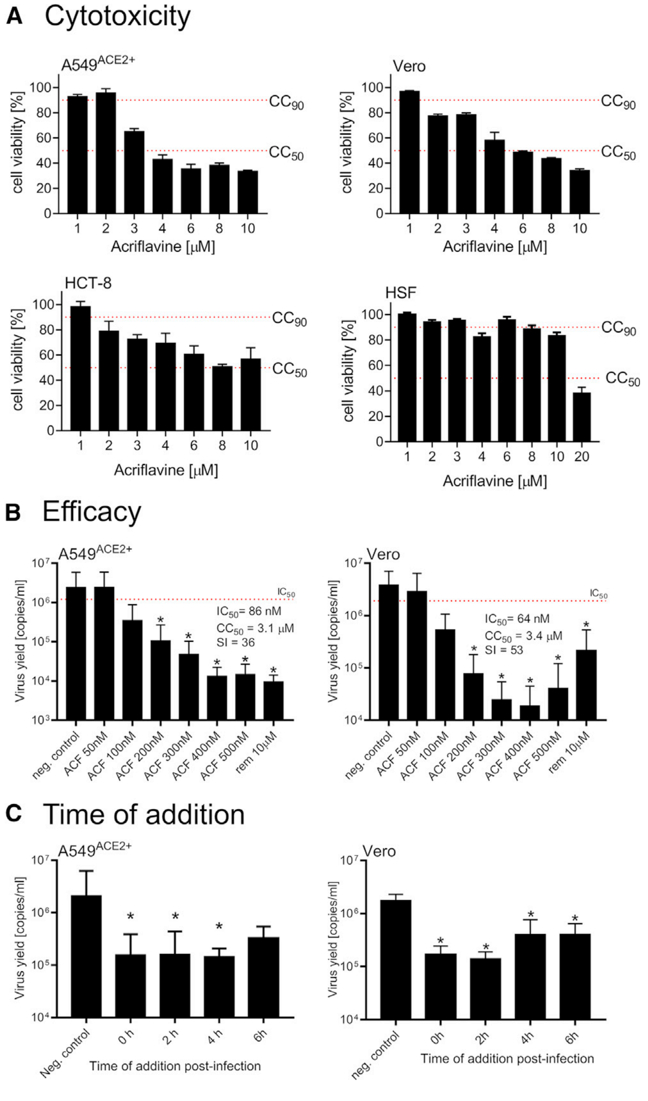

Figure 3. ACF inhibits SARS-CoV-2 replication *in vitro*

(A) Cytotoxicity of ACF in four cell culture systems employing cell lines ($A549^{ACE2+}$, Vero cells, HCT-8 cells) and primary human skin fibroblasts (HSF).
(B) Inhibition of virus replication by ACF in $A549^{ACE2+}$ (left) and Vero (right) cells. The figure shows qRT-PCR analysis of cell culture supernatants infected with SARS-CoV-2 at 1,600 $TCID_{50}$/mL 24 h post-infection.
(C) Time-of-addition study. The inhibition of virus replication in $A549^{ACE2+}$ cells (left) or Vero cells (right) by ACF added at different times post-infection (time denoted on the x axis). The figure shows qRT-PCR analysis of cell culture supernatants infected with SARS-CoV-2 at 1,600 $TCID_{50}$/mL) 24 h post-infection. All experiments were performed in at least three biological repetitions, each in triplicate. The results are presented as average values with standard deviations (error bars). *Significantly different from the control ($p < 0.05$).

To understand the molecular basis of the SARS-CoV2-PL^{pro} inhibition by ACF, we determined the X-ray crystal structure of the protease in complex with proflavine (PDB: 7NT4), one of the principal active components of ACF. Analysis of the electron-density map shows that two molecules (occupancy = 1.0) of proflavine are π-π stacked to each other and accommodate the S3–S5 pockets of the PL^{pro} substrate-recognition cleft, which is defined by the loop connecting helices α3 and α4 and the so-called "blocking loop" BL2 (Figure 2B) (Ratia et al., 2006). Comparison with the apo structure of PL^{pro} (PDB: 7D47) revealed that, although the overall structure is well preserved, the BL2 loop undergoes a large conformational change upon binding of the ligand. In particular, the side chain of Tyr268 rotates by around 57° inward toward the substrate-recognition cleft, and the BL2 loop moves by 2 Å in the same direction, narrowing the substrate-binding cleft (Figure S3).

Several PL^{pro} residues are involved in ligand binding. One of the molecules, termed proflavine-I, occupies the S4 pocket (Figures 2B–2D). The side chain Tyr273 is involved in a hydrogen bond (2.9 Å), with the primary amine group at position 3 of proflavine-I, which sits at the bottom of the substrate-binding cleft, where it forms a T-stacked CH/π interaction with Pro247 (3.9 Å). A parallel stacking CH/π interaction with Pro248 (4.6 Å) and T-shaped π-π stacking with the aromatic side chain of Tyr264 is engaged in a T-shaped π-π stacking interaction (3.5 Å), further stabilizing the interaction with proflavine-I. The second molecule, termed proflavine-II, shows π-π stacking at 3.5 Å with proflavine-I and occupies the S3 and S5 pockets (Figures 2D and 2E). Gly163 and Asp164 form hydrogen bonds with the primary amine group at position 3 (2.9 Å) and the imino group of the acridine moiety (2.9 Å), respectively. In addition, Tyr268 forms a T-shaped π-π stacked interaction (5.1 Å) with proflavine-II. Overall, this provides a unique binding mode, where two proflavines, tightly π-π stacked, cooperate in blocking the substrate pocket. Importantly, both molecules are required for the inhibition.

Recently, Shin et al. reported the crystal structure of SARS-CoV2-PL^{pro} in complex with ISG15 (interferon-induced gene 15) bearing the RLRGG recognition motif at the C terminus (Shin et al., 2020). Comparison with our structure shows that the proflavine-II molecule, which occupies the S3 and S5 pockets, overlaps very well with the backbone of Arg151 and Arg153 in the RLRGG peptide in positions P3 and P5, respectively (Figures 2E and 2F). The side chain of Leu152 in position P4 points exactly toward the other molecule of proflavine in the S4 pocket. All the major interactions of the substrate with PL^{pro} residues are recapitulated by the inhibitor. Mechanistically, these observations indicate that proflavine inhibits SARS-CoV2-PL^{pro} by limiting access to the substrate-binding site. Moreover, the fact that the imino group of the proflavine-I molecule in the S4 pocket is not involved in any polar interactions suggests that the methylated (ACF) form is preferred at this position due to lack of desolvation penalty. The amino group at position 3 of proflavine-II is located in a position similar to that of the amide nitrogen of the RLRGG glycine P2 in the P2 pocket. Side-methylated proflavine, which is also present in commercial ACF preparations, would, therefore, mimic the P2 amino acid. Intriguingly, a unique feature of the commercial ACF mixtures is that they contain the combination of differently methylated proflavines to optimally block the PL^{pro} active site.

ACF activity in SARS-CoV-2-infected cell culture

For cellular validation of ACF activity, two SARS-CoV-2 infection cell culture models were used: Vero cells, which are a broadly used simian model, and human $A549^{ACE2+}$ cells overexpressing the angiotensin-converting enzyme 2 (ACE2) receptor (Milewska et al., 2020). First, the cytotoxicity of ACF was evaluated on a larger cell line panel ($A549^{ACE2+}$, Vero, HCT-8, CRFK) as well

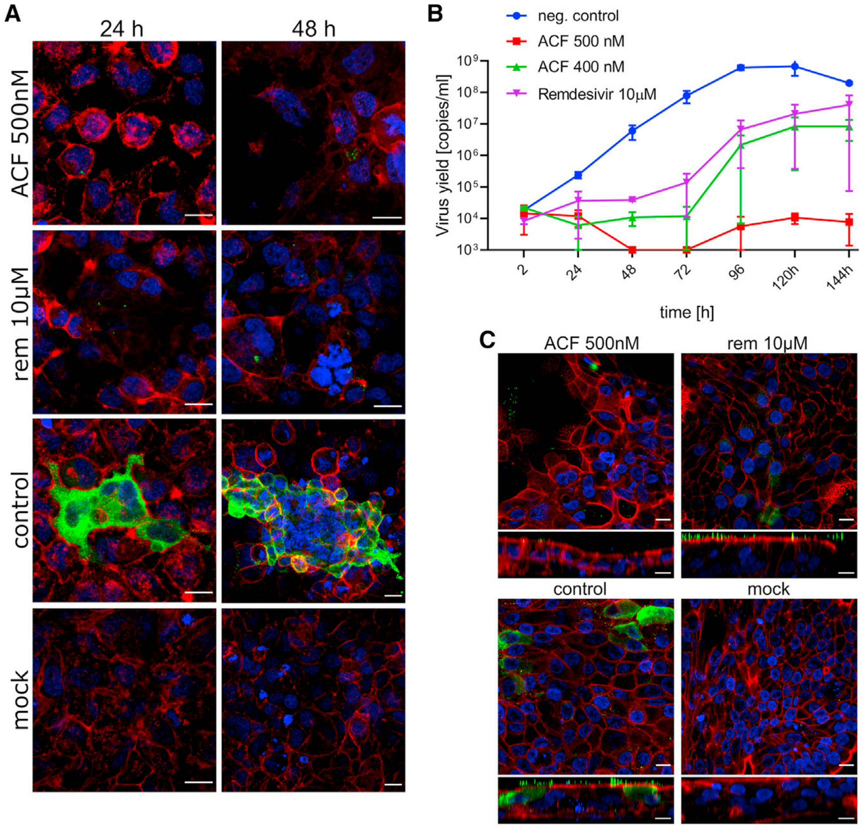

Figure 4. ACF blocks SARS-CoV-2 replication *in vitro* and *ex vivo*

(A) Inhibition of virus replication by ACF in A549^{ACE2+} cells visualized with confocal microscopy. Cells were infected with SARS-CoV-2 in the presence of 500 nM ACF, 10 μM remdesivir (REM), or vehicle control (control) for 24 and 48 h. Cell nuclei are denoted in blue, actin is denoted in red, and SARS-CoV-2 N protein is denoted in green. Each image represents maximum projection of a 5 μm section. Scale bar, 20 μm.

(B) Antiviral activity of ACF against SARS-CoV-2 in human airway epithelium (MucilAir). The figure shows qRT-PCR analysis of HAE culture supernatants infected with SARS-CoV-2. REM and PBS were used as controls. The assay was performed at least in duplicate, and median values with range are presented. Two-way ANOVA with Dunnett's *post hoc* test indicated that ACF and REM significantly inhibited virus yields during infection course compared with untreated control.

(C) Confocal analysis of infected HAE cultures. Cells were infected with SARS-CoV-2 in the presence of 500 nM ACF, 10 μM REM, or vehicle control (control). Mock images illustrate non-infected cells. On day 6 post-infection, cells were fixed and immunostained. Cell nuclei are denoted in blue, actin is denoted in red, and SARS-CoV-2 N protein is denoted in green. Each image represents maximum projection of a 3 μm section. Scale bar, 10 μm.

as on primary human fibroblasts (Figures 3A and S4A). The cellular cytotoxicity CC_{50} values were determined in both cell types to be 3.1 μM for A549^{ACE2+}, 3.4 μM for Vero, 2.1 μM for HCT-8, and 12 μM for primary human fibroblasts. Interestingly, ACF shows lower cytotoxicity in primary cells compared with transformed cell lines, which may reflect the previously described antineoplastic activity of ACF (Lee et al., 2014). Second, dose-response experiments were carried out in A549^{ACE2+} and Vero cells (Figure 3B). The IC_{50} values determined for ACF are 86 and 64 nM for A549^{ACE2+} cells and Vero cells, respectively. Accordingly, the selectivity index (SI) values for A549^{ACE2+} and Vero cells are 36 and 53, thus representing a potent inhibitor of SARS-CoV-2 virus replication with a favorable cytotoxicity profile. Notably, ACF inhibition at 400 nM is significantly more effective than inhibition by remdesivir at a 25-fold higher concentration in these assays (Figure 3B). The decrease in virus yields was observed for both cell culture supernatants and lysates (Figure S4B). The results were also verified using the viral plaque assay (Figure S4C).

Next, we carried out time-of-addition experiments, where cells (A549^{ACE2+} and Vero cells) were first infected with the virus, and the ACF was added after 0, 2, 4, or 6 h. The results show that virus inhibition was maintained, even when the compound was not present during the early stages of infection. Consequently, we conclude that SARS-CoV-2 is mainly inhibited during the replication phase, and ACF does not affect viral entry (Figure 3C).

Inhibition of virus replication by ACF was further confirmed using confocal microscopy. Twenty-four and 48 h post-infection in the presence or absence of 500 nM ACF or 10 μM remdesivir, confocal microscopy images showed nearly complete elimination of SARS-CoV-2 compared with untreated cells. Although virus elimination is also observed for remdesivir, this is seen only at more than 20-fold higher concentrations compared with ACF (Figure 4A).

We further analyzed whether ACF as a protease inhibitor may show a synergistic effect when administered together with remdesivir, a replication inhibitor. The synergistic effect was assayed by infecting Vero cells in the presence of ACF and remdesivir, as described under STAR Methods. The results are presented in Figures S5A and S5B. The IC_{50} dose of remdesivir in our model was 85 nM and for ACF 64 nM. Calculated IC_{50} doses of tested compounds obtained in combination with IC_{50}/2 doses of ACF and remdesivir were significantly lower than those of the compounds alone (2.26 nM for remdesivir [REM] and 6.5 nM for ACF). The calculated combination index (CI) of 0.13 suggests that these two compounds exhibit a very strong synergic effect in the inhibition of SARS-CoV-2 replication *in vitro*.

Ex vivo inhibition of SARS-CoV-2 infection in HAE cultures

The antiviral activity of ACF was analyzed in the HAE *ex vivo* model. Two different concentrations were evaluated (400 and 500 nM); PBS and remdesivir were used as controls. The results (Figures 4B and S5C) show inhibition of SARS-CoV-2 replication in the presence of ACF and remdesivir in the HAE

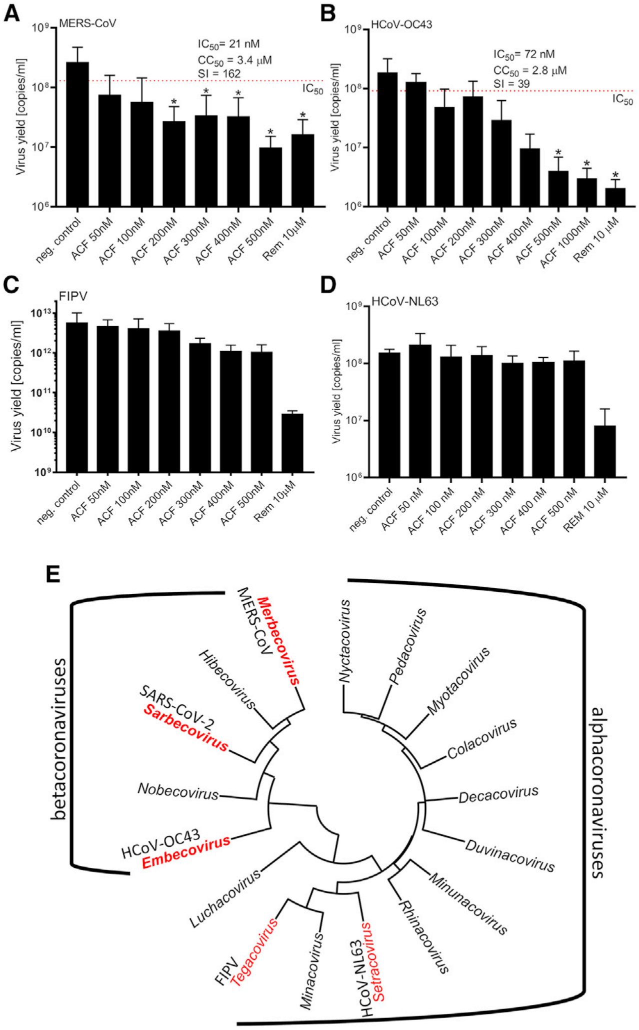

Figure 5. ACF is a broad-spectrum inhibitor of betacoronaviruses

(A–D) Replication of (A) MERS-CoV, (B) HCoV-OC43, (C) FIPV, and (D) HCoV-NL63 *in vitro* in the presence or absence of inhibitors, as assessed with qRT-PCR on cell culture supernatants. A single round of infection was recorded (24 h). All experiments were performed in at least two biological repetitions, each in triplicate. The results are presented as average values with standard deviations (error bars). *Significantly different from the untreated control ($p < 0.05$). ACF, acriflavine; Rem, remdesivir. (E) Phylogenetic tree of alpha- and betacoronaviruses. Representative alpha- and betacoronavirus genera considered in this study are highlighted in red.

ex vivo model. A significantly lower viral yield was detected in the cultures treated with ACF compared with the PBS control. ACF (500 nM)-treated HAE showed higher inhibition of virus replication than the positive control remdesivir at 10 μM concentration after 144 h of infection. At time points of 48 and 72 h of infection, the virus was beyond detection limits in the ACF 500 nM-treated sample. The IC$_{50}$ values for ACF in HAE cultures are provided in Table S4.

After 6 days of infection in the presence of 500 nM ACF, confocal microscopy images showed complete inhibition of SARS-CoV-2 replication. Although inhibition was also noted for remdesivir, the virus particles in the remdesivir-treated cells were still present on the cell surface, suggesting that a detectable level of virions was still being produced. Therefore, the inhibition by 10 μM remdesivir was inferior compared with 500 nM ACF (Figure 4C).

Pan-coronavirus activity of ACF

To verify whether ACF may be used as a broadband anticoronaviral drug, its activity was tested against betacoronaviruses other than SARS-CoV-2, i.e., MERS-CoV and HCoV-OC43, as well as alphacoronaviruses, i.e., HCoV-NL63 and feline infectious peritonitis virus (FIPV). ACF efficiently inhibited MERS-CoV (IC$_{50}$ = 21 nM, SI = 162) and HCoV-OC43 (IC$_{50}$ = 105 nM, SI = 27). Interestingly, no effect on the replication of tested alphacoronaviruses was observed (Figure 5). This can be explained on the basis of amino acid sequence differences of PL^{pro} encoded by alpha- and betacoronaviruses: alphacoronaviruses lack a stretch of 40 amino acids that mediates crucial interactions with the proflavines (Figure S6). This difference further corroborates the fact that ACF acts by inhibition of the SARS-CoV-2 PL^{pro} protease and not by other potential mechanisms. The high sequence identity among SARS-CoV2-PL^{pro} across betacoronaviruses indicates that ACF can be used as an antiviral compound for betacoronaviruses in general, and thus could represent a drug ready to use for future outbreaks.

ACF administration can achieve therapeutic doses in lungs

The pharmacokinetics of ACF has been previously reported in the context of its antitumor activity. The published data point to a very fast plasma clearance of ACF by intravenous and intramuscular delivery (Lee et al., 2007; Shin et al., 2008). ACF is approved for oral use as a systemic drug against urinary tract infections in Brazil; yet, data on oral bioavailability, pharmacokinetics, and lung concentration levels of ACF are not publicly available. To explore if oral administration can reach therapeutic levels in lungs, we measured the pharmacokinetics of all four major components of commercial ACF (see supplementary analysis of ACF composition) in mice following intravenous and oral administration. Our data indicate that proflavine compounds (non-methylated at the heterocyclic nitrogen) are highly bioavailable, whereas methylation of this position significantly limits oral bioavailability. The data also confirm very fast plasma clearance (Figure 6) following intravenous administration, mainly mediated by high volume of distribution. Thus, the levels of proflavine and side-methylated proflavine in lungs remained high and stable for a prolonged period of time. Two hours after administration, the lung concentrations of proflavine were 22 and 67 μM for intravenous and oral delivery, respectively. These levels of the inhibitor are at least two orders of magnitude higher than the therapeutic dose observed *in vitro*. Therefore, the approved dosage in the range of single-digit milligrams per kilogram is expected to achieve a therapeutic effect. Components of ACF methylated in the central aromatic ring were not orally available. However, proflavine and side-methylated proflavine are active against SARS-CoV-2 *in vitro*. Therefore, we infer that commercial ACF mixtures dosed at concentrations approved for clinical use could be used orally to treat SARS-CoV-2. Detailed information on exposure parameters is provided in Table S5.

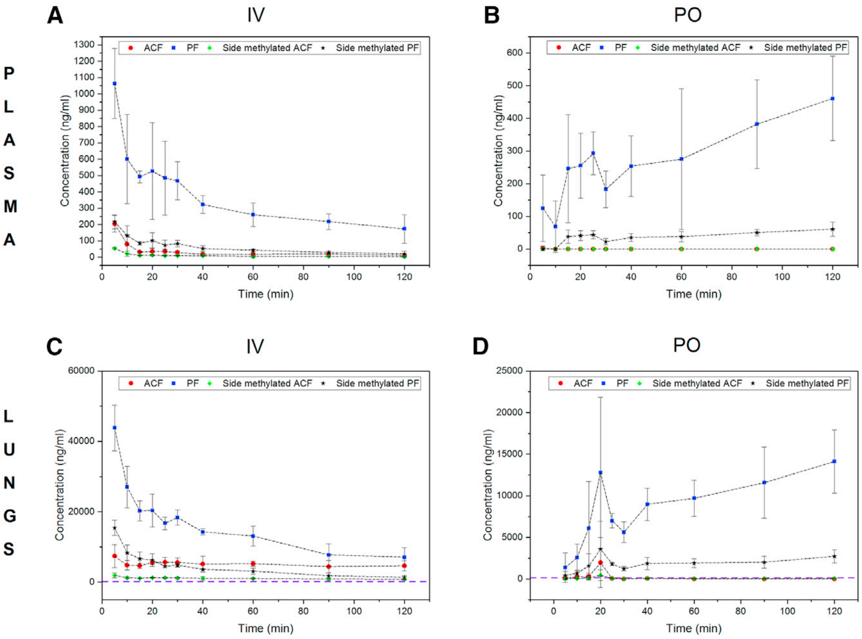

Figure 6. Pharmacokinetic study of ACF in CD-1 mice

(A–D) The mice were given a single dose intravenously (IV; A and C) (15 mg/kg) and orally (PO; B and D) (100 mg/kg) of the commercially available drug composed of ACF, proflavine (PF), side-methylated ACF, and side-methylated PF. Plasma concentrations (A and B) and lung concentrations (C and D) are shown. Purple dashed lines indicate the ACF concentration (112 ng/mL) needed to inhibit the viral replication in HAE cultures. PF and side-methylated PF have much higher bioavailability, and lung exposure to these components is very high. Each of the time point treatment group included 4 animals. Error bars have been calculated as standard deviation of values measured at respective time point.

Effect of ACF in an *in vivo* model of infection

To confirm that ACF can block virus replication *in vivo*, we used an infection model based on K18-ACE2 mice. The experiment groups consisted of infection control receiving no treatment, ACF administered orally (p.o.; 100 mg/kg daily), two groups receiving ACF intramuscularly (i.m.; 5 mg/kg or 15 mg/kg body wt twice a day), and a positive control group receiving remdesivir (i.m.; 25 mg/kg per day). The administration of the ACF and remdesivir started 1 day prior to infection with SARS-CoV-2 virus. The treatment was continued for 6 consecutive days.

In all groups, the animals survived the infection until the last day, and no apparent signs of the disease were noted, including the lack of change in body weight. There were also no drug-related adverse effects. Analysis of the virus replication levels by qRT-PCR on day 6 in the untreated group clearly showed that the virus replicated in lungs and brains. Treatment with ACF (both p.o. and i.m.) almost completely blocked the infection in the brain (Figure 7A), whereas the positive control remdesivir decreased the viral loads by only 2–3 orders of magnitude. The infection levels were less pronounced in the lungs, but suppressed replication of the virus was also recorded for the treatment groups, with the most pronounced effect (1–2 orders of magnitude reduction) observed for the p.o. administration of ACF (Figure 7B).

DISCUSSION

SARS-CoV-2 is the cause of the most devastating global pandemic since the 1918 influenza. Despite extensive research, early efforts failed to deliver effective antivirals to control the infection. Drugs inhibiting virus replication should be given early during the infection, but the required early diagnosis and the availability and costs involved render this challenging. A cheap, easily accessible drug like ACF might offer the required early availability and accessibility. Moreover, our data show that ACF can be used as part of a combination therapy strategy (Lu et al., 2018), as we observe a strong synergy between ACF and the currently used remdesivir in inhibiting viral replication.

Here, we focused on one of the viral proteases, PL^{pro}, which is indispensable for SARS-CoV-2 replication, progeny production, and attenuation of the host's immune responses (Knipe and Howley, 2013; Shin et al., 2020). PL^{pro} modulates the ISGylation pathway, which acts as a viral defense mechanism to inhibit normal protein translation. ISGylation modifies protein kinase R, so that newly synthesized (viral) proteins are tagged as dangerous (Villarroya-Beltri et al., 2017). Inhibition of PL^{pro} will not only interfere with virus protein maturation but also activate the host cellular defense mechanisms to fight SARS-CoV-2 infection.

We show that ACF is a potent, specific inhibitor of PL^{pro}, with IC_{50} values in the low nanomolar range in all tested cell models. The activity is promising and by far exceeds the reported activities for GRL-0617 (Shin et al., 2020) and rac5c (Klemm et al., 2020), both active at the micromolar range. Structural analysis revealed that the inhibitor blocks the catalytic site of the PL^{pro}. An unexpected and highly unusual mechanism of inhibition is observed, where two ACF molecules bind in the enzyme's substrate-binding site. The crystal structure and validation of binding in solution using NMR confirm the mode of action of ACF. Together with the high potency in cellular models, these findings identify ACF as a highly attractive repurposing molecule to inhibit SARS-CoV-2 replication.

Despite a relatively short half-life for ACF *in vivo* (Song et al., 2005), we have observed a reduction of several orders of magnitude in viral load in a humanized mouse infection model. This suggests that with the development of the correct treatment regimen, the therapeutic effect of ACF can be extended in humans.

Notably, in addition to SARS-CoV-2, the antiviral effect of ACF was observed for other betacoronaviruses, MERS-CoV and HCoV-OC43, but not for other genera of the *Coronaviridae* family (alphacoronaviruses). We believe that these data indicate a broad-spectrum activity of ACF against betacoronaviruses, with the potential to target future zoonotic coronaviruses. This

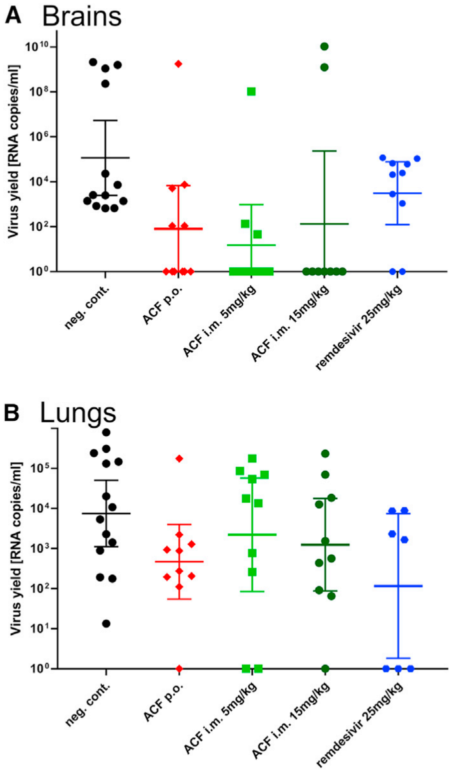

Figure 7. Inhibition of virus replication by ACF *in vivo*

Each group consisted of 10 animals, except for the reference group, where 15 animals were included. Oral and intramuscular delivery were tested. Remdesivir was used as positive control. Virus replication in different organs was assessed using RT-qPCR. A strong reduction of virus level is visible in the brain of treated groups. ACF caused a marked reduction of virus load in the lungs when administered orally. Data are presented as geometric mean with 95% confidence intervals.

means that ACF not only has therapeutic benefits in the current crisis, but also can become an important component of the arsenal against future pandemics.

The unique and specific inhibition of SARS-CoV-2 PL^{pro} and associated inhibition of virus replication in the cell culture, *ex vivo* and *in vivo*, renders ACF an attractive compound for evaluation in the treatment of COVID-19. It has to be considered, however, that the aromatic acridine rings in ACF are linked with DNA-intercalating properties and thus exhibit mutagenic potential. On the other hand, a substantial amount of long-term clinical data is available for systematic applications of ACF (Gama et al., 2020; Mathé et al., 1996, 1998), thus alleviating concerns related to the potential mutagenic effects, especially for short-term antiviral therapy. Importantly, the antiviral effects are observed at concentrations of 2–3 orders of magnitude lower than those used in experiments assessing *in vitro* mutagenicity of ACF (Obstoy et al., 2015; Rees et al., 1989).

In conclusion, we have identified a potent small-molecule inhibitor of the coronaviral PL^{pro} that is registered and marketed as an inexpensive over-the-counter drug. The low-nanomolar IC_{50} and good SI, combined with the profound inhibition of the viral replication in all tested models, suggest that the drug may be effective in monotherapy or in combination therapy with, e.g., polymerase inhibitors. ACF may be administered early during the infection, considering the risk/benefit ratio for a particular patient. Specifically, an elderly patient population may significantly benefit from a new antiviral treatment option, as mortality in the age group 70+ years is significantly increased compared with younger groups. In addition, the antiviral effect against other betacoronaviruses argues that further research into the therapeutic potential of ACF may provide protection against future zoonotic infections of betacoronaviruses. The unique mode of inhibition of ACF will also serve as a blueprint to develop new, improved drugs with a broadband activity using structure-based drug development to prepare for future coronavirus outbreaks.

SIGNIFICANCE

Here, we describe the identification and comprehensive validation of acriflavine as a potent and highly specific inhibitor of the SARS-CoV-2 papain-like protease (PL^{pro}). The drug is cheap and readily available in some countries as an over-the-counter medicine. Despite the chemical structure of the compound, the safety has been established in clinical trials in recent years.

STAR★METHODS

Detailed methods are provided in the online version of this paper and include the following:

- KEY RESOURCES TABLE
- RESOURCE AVAILABILITY
    - ○ Lead contact
    - ○ Materials availability
    - ○ Data and code availability
- EXPERIMENTAL MODEL AND SUBJECT DETAILS
    - ○ Animal studies
    - ○ Cells
    - ○ Viruses
- METHOD DETAILS
    - ○ Plasmids and proteins
    - ○ PL^{pro} activity assay
    - ○ M^{pro} activity assay
    - ○ Compound screening
    - ○ PL^{pro} inhibitor IC_{50} determination
    - ○ Gel-based PL^{pro} DUB activity
    - ○ Chemical characterization of the ACF components
    - ○ Cell viability assay
    - ○ Isolation of nucleic acids, RT-qPCR
    - ○ Virus replication inhibition assay
    - ○ Plaque assay
    - ○ Synergistic action of AFC and remdesivir
    - ○ Phylogenetic analysis
    - ○ Virus visualization
    - ○ Pharmacokinetics study of ACF in CD-1 mice
    - ○ Animal study
    - ○ NMR spectroscopy
    - ○ Crystallization and structure solution
- QUANTIFICATION AND STATISTICAL ANALYSIS

SUPPLEMENTAL INFORMATION

Supplemental information can be found online at https://doi.org/10.1016/j.chembiol.2021.11.006.

ACKNOWLEDGMENTS

This work was supported by a subsidy from the Polish Ministry of Science and Higher Education for research on SARS-CoV-2 and a grant from the National Science Center (UMO-2017/27/B/NZ6/02488) and by EU-Horizon2020 ITN OrganoVir grant 812673 (to K.P). Support by the Bayerische Forschungsstiftung grant AZ-1453-20C (to M.S. and G.P.) is acknowledged. K.O. was supported by the Foundation for Polish Science.

AUTHOR CONTRIBUTIONS

Conceptualization, M.S., K.H., G.P., and K.P.; methodology, formal analysis, and investigation, V.N., K.S., F.S., A.M., A.D., E.B.D., M.B., P.B., Y.C., A.C., G.D., K.O., M.P., J.P., A.S., K.G.I.M., B.B., G.P., and K.P.; writing – original draft, K.P., G.P., K.H., and M.S.; writing – review & editing, all authors; funding acquisition and supervision, M.S., K.H., G.P., and K.P.

DECLARATION OF INTERESTS

ACF and its derivatives and their use against betacoronaviruses are protected by European patent application no. 20214108.1, submitted by the authors of this paper. Disclosure statement: M.J.B. is a current employee of AstraZeneca.

Received: July 17, 2021
Revised: September 29, 2021
Accepted: November 29, 2021
Published: May 19, 2022

SUPPORTING CITATIONS

The following references appear in the supplemental information: Robert and Gouet (2014).

REFERENCES

Benzekri, R., Bouslama, L., Papetti, A., Hammami, M., Smaoui, A., and Limam, F. (2018). Anti HSV-2 activity of Peganum harmala (L.) and isolation of the active compound. Microb. Pathog. *114*, 291–298. https://doi.org/10.1016/j.micpath.2017.12.017.

Browning, C.H. (1943). Aminoacridine compounds as surface antiseptics. Br. Med. J. *1*, 341–343. https://doi.org/10.1136/bmj.1.4289.341.

Browning, C.H. (1967). Proflavine and acriflavine. Br. Med. J. *2*, 111. https://doi.org/10.1136/bmj.2.5544.111-a.

Brünger, A.T. (1992). Free R value: a novel statistical quantity for assessing the accuracy of crystal structures. Nature *355*, 472–475. https://doi.org/10.1038/355472a0.

Cao, B., Wang, Y., Wen, D., Liu, W., Wang, J., Fan, G., Ruan, L., Song, B., Cai, Y., Wei, M., et al. (2020). A trial of lopinavir-ritonavir in adults hospitalized with severe Covid-19. N. Engl. J. Med. *382*, 1787–1799. https://doi.org/10.1056/NEJMoa2001282.

Capasso, C., Nocentini, A., and Supuran, C.T. (2020). Protease inhibitors targeting the main protease and papain-like protease of coronaviruses. Expert Opin. Ther. Pat, 1–16. https://doi.org/10.1080/13543776.2021.1857726.

Corsello, S.M., Bittker, J.A., Liu, Z., Gould, J., McCarren, P., Hirschman, J.E., Johnston, S.E., Vrcic, A., Wong, B., Khan, M., et al. (2017). The Drug Repurposing Hub: a next-generation drug library and information resource. Nat. Med. *23*, 405–408. https://doi.org/10.1038/nm.4306.

Dana, S., Prusty, D., Dhayal, D., Gupta, M.K., Dar, A., Sen, S., Mukhopadhyay, P., Adak, T., and Dhar, S.K. (2014). Potent antimalarial activity of acriflavine in vitro and in vivo. ACS Chem. Biol. *9*, 2366–2373. https://doi.org/10.1021/cb500476q.

Drosten, C., Günther, S., Preiser, W., van der Werf, S., Brodt, H.R., Becker, S., Rabenau, H., Panning, M., Kolesnikova, L., Fouchier, R.A., et al. (2003). Identification of a novel coronavirus in patients with severe acute respiratory syndrome. N. Engl. J. Med. *348*, 1967–1976. https://doi.org/10.1056/NEJMoa030747.

Emsley, P. (2017). Tools for ligand validation in Coot. Acta Crystallogr. D Struct. Biol. *73*, 203–210. https://doi.org/10.1107/s2059798317003382.

Emsley, P., and Cowtan, K. (2004). Coot: model-building tools for molecular graphics. Acta Crystallogr. D Biol. Crystallogr. *60*, 2126–2132. https://doi.org/10.1107/s0907444904019158.

Funatsuki, K., Tanaka, R., Inagaki, S., Konno, H., Katoh, K., and Nakamura, H. (1997). acrB mutation located at carboxyl-terminal region of gyrase B subunit reduces DNA binding of DNA gyrase. J. Biol. Chem. *272*, 13302–13308. https://doi.org/10.1074/jbc.272.20.13302.

Gama, C.R.B., Nunes, C.P., Gama, G.F., Mezitis, S.G.E., Suchmacher Neto, M., Guimarães, O.R., Geller, M., Oliveira, L., de Souza da Fonseca, A., Sitnoveter, A., et al. (2020). Treatment of recurrent urinary tract infection symptoms with urinary antiseptics containing methenamine and methylene blue: analysis of etiology and treatment outcomes. Res. Rep. Urol. *12*. https://doi.org/10.2147/RRU.S279060.

Horby, P., Mafham, M., Linsell, L., Bell, J.L., Staplin, N., Emberson, J.R., Wiselka, M., Ustianowski, A., Elmahi, E., Prudon, B., et al. (2020). Effect of hydroxychloroquine in hospitalized patients with Covid-19. N. Engl. J. Med. *383*, 2030–2040. https://doi.org/10.1056/NEJMoa2022926.

Iacobucci, G. (2020). Covid-19: risk of death more than doubled in people who also had flu, English data show. BMJ *370*, m3720. https://doi.org/10.1136/bmj.m3720.

Kabsch, W. (2010). Xds. Acta Crystallogr. D Biol. Crystallogr. *66*, 125–132. https://doi.org/10.1107/s0907444909047337.

Kawai, M., and Yamagishi, J. (2009). Mechanisms of action of acriflavine: electron microscopic study of cell wall changes induced in Staphylococcus aureus by acriflavine. Microbiol. Immunol. *53*, 481–486. https://doi.org/10.1111/j.1348-0421.2009.00151.x.

Klemm, T., Ebert, G., Calleja, D.J., Allison, C.C., Richardson, L.W., Bernardini, J.P., Lu, B.G., Kuchel, N.W., Grohmann, C., Shibata, Y., et al. (2020). Mechanism and inhibition of the papain-like protease, PLpro, of SARS-CoV-2. Embo J. *39*, e106275. https://doi.org/10.15252/embj.2020106275.

Knipe, D.M., and Howley, P.M. (2013). Fields Virology, 6th Edition (Wolters Kluwer/Lippincott Williams & Wilkins Health).

Ksiazek, T.G., Erdman, D., Goldsmith, C.S., Zaki, S.R., Peret, T., Emery, S., Tong, S., Urbani, C., Comer, J.A., Lim, W., et al. (2003). A novel coronavirus associated with severe acute respiratory syndrome. N. Engl. J. Med. *348*, 1953–1966. https://doi.org/10.1056/NEJMoa030781.

Kumar, S., Stecher, G., Li, M., Knyaz, C., and Tamura, K. (2018). Mega X: molecular evolutionary genetics analysis across computing platforms. Mol. Biol. Evol. *35*, 1547–1549. https://doi.org/10.1093/molbev/msy096.

Lee, C.J., Yue, C.H., Lin, Y.J., Lin, Y.Y., Kao, S.H., Liu, J.Y., and Chen, Y.H. (2014). Antitumor activity of acriflavine in lung adenocarcinoma cell line A549. Anticancer Res. *34*, 6467–6472.

Lee, K., Zhang, H., Qian, D.Z., Rey, S., Liu, J.O., and Semenza, G.L. (2009). Acriflavine inhibits HIF-1 dimerization, tumor growth, and vascularization. Proc. Natl. Acad. Sci. U S A *106*, 17910–17915. https://doi.org/10.1073/pnas.0909353106.

Lee, P.S., Shin, D.H., Lee, K.M., Song, S., Yoo, H.S., Moon, D.C., Hong, J.T., and Chung, Y.B. (2007). Effects of guanosine on the pharmacokinetics of acriflavine in rats following the administration of a 1:1 mixture of acriflavine and guanosine, a potential antitumor agent. Arch. Pharm. Res. *30*, 372–380. https://doi.org/10.1007/BF02977621.

Lu, D.Y., Wu, H.Y., Yarla, N.S., Xu, B., Ding, J., and Lu, T.R. (2018). HAART in HIV/AIDS treatments: future trends. Infect Disord. Drug Targets *18*, 15–22. https://doi.org/10.2174/1871526517666170505122800.

Ma, L., Wang, W., Le Grange, J.M., Wang, X., Du, S., Li, C., Wei, J., and Zhang, J.N. (2020). Coinfection of SARS-CoV-2 and other respiratory pathogens. Infect Drug Resist *13*, 3045–3053. https://doi.org/10.2147/idr.S267238.

Manchester, T., Cavalcanti, D.P., Zogovich, M., W, D.E.S., and Motta, M.C. (2013). Acriflavine treatment promotes dyskinetoplasty in Trypanosoma cruzi as revealed by ultrastructural analysis. Parasitology *140*, 1422–1431. https://doi.org/10.1017/s0031182013001029.

Mathé, G. (2000). The non-enumerable described retrovirus integrase inhibitors are not a lure, as evidenced by ten years of clinical experience. Biomed. Pharmacother. *54*, 3–6. https://doi.org/10.1016/S0753-3322(00)88633-3.

Mathé, G., Pontiggia, P., Orbach-Arbouys, S., Triana, K., Ambetima, N., Morette, C., Hallard, M., and Blanquet, D. (1996). AIDS therapy with two, three or four agent combinations, applied in short sequences, differing from each other by drug rotation. I. First of two parts: a phase I trial equivalent, concerning five virostatics: AZT, ddI, ddC, acriflavine and an ellipticine analogue. Biomed. Pharmacother. *50*, 220–227. https://doi.org/10.1016/0753-3322(96)87662-1.

Mathé, G., Triana, K., Pontiggia, P., Blanquet, D., Hallard, M., and Morette, C. (1998). Data of pre-clinical and early clinical trials of acriflavine and hydroxy-methyl-ellipticine reviewed, enriched by the experience of their use for 18 months to 6 years in combinations with other HIV1 virostatics. Biomed. Pharmacother. *52*, 391–396. https://doi.org/10.1016/s0753-3322(99)80007-9.

McCoy, A.J. (2007). Solving structures of protein complexes by molecular replacement with Phaser. Acta Crystallogr. D Biol. Crystallogr. *63*, 32–41. https://doi.org/10.1107/s0907444906045975.

McCoy, A.J., Grosse-Kunstleve, R.W., Adams, P.D., Winn, M.D., Storoni, L.C., and Read, R.J. (2007). Phaser crystallographic software. J. Appl. Crystallogr. *40*, 658–674. https://doi.org/10.1107/s0021889807021206.

Milewska, A., Chi, Y., Szczepanski, A., Barreto-Duran, E., Dabrowska, A., Botwina, P., Obloza, M., Liu, K., Liu, D., Guo, X., et al. (2020). HTCC as a polymeric inhibitor of SARS-CoV-2 and MERS-CoV. J. Virol. https://doi.org/10.1128/JVI.01622-20.

Milewska, A., Zarebski, M., Nowak, P., Stozek, K., Potempa, J., and Pyrc, K. (2014). Human coronavirus NL63 utilizes heparan sulfate proteoglycans for attachment to target cells. J. Virol. *88*, 13221–13230. https://doi.org/10.1128/JVI.02078-14.

Mirzaei, R., Goodarzi, P., Asadi, M., Soltani, A., Aljanabi, H.A.A., Jeda, A.S., Dashtbin, S., Jalalifar, S., Mohammadzadeh, R., Teimoori, A., et al. (2020). Bacterial co-infections with SARS-CoV-2. IUBMB Life. https://doi.org/10.1002/iub.2356.

Murshudov, G.N., Skubák, P., Lebedev, A.A., Pannu, N.S., Steiner, R.A., Nicholls, R.A., Winn, M.D., Long, F., and Vagin, A.A. (2011). REFMAC5 for the refinement of macromolecular crystal structures. Acta Crystallogr. D Biol. Crystallogr. *67*, 355–367. https://doi.org/10.1107/s0907444911001314.

NCT03379389 (2020). Clinical assessment of urinary antiseptics methenamine and methylthioninium in recurrent cystitis. https://clinicaltrials.gov/ct2/show/NCT03379389.

Nehme, R., Hallal, R., El Dor, M., Kobeissy, F., Gouilleux, F., Mazurier, F., and Zibara, K. (2020). Repurposing of acriflavine to target chronic myeloid Leukemia treatment. Curr. Med. Chem. https://doi.org/10.2174/0929867327666200908114411.

Nei, M., and Kumar, S. (2000). Molecular Evolution and Phylogenetics (Oxford University Press).

Nietlispach, D. (2005). Suppression of anti-TROSY lines in a sensitivity enhanced gradient selection TROSY scheme. J. Biomol. NMR *31*, 161–166. https://doi.org/10.1007/s10858-004-8195-7.

Obstoy, B., Salaun, M., Veresezan, L., Sesboüé, R., Bohn, P., Boland, F.-X., and Thiberville, L. (2015). Safety and performance analysis of acriflavine and methylene blue for in vivo imaging of precancerous lesions using fibered confocal fluorescence microscopy (FCFM): an experimental study. BMC Pulm. Med. *15*, 30. https://doi.org/10.1186/s12890-015-0020-4.

Pan, H., Peto, R., Henao-Restrepo, A.M., Preziosi, M.P., Sathiyamoorthy, V., Abdool Karim, Q., Alejandria, M.M., Hernández García, C., Kieny, M.P., Malekzadeh, R., et al. (2020). Repurposed antiviral drugs for covid-19 - interim who solidarity trial results. N. Engl. J. Med. https://doi.org/10.1056/NEJMoa2023184.

Parker, E.P.K., Shrotri, M., and Kampmann, B. (2020). Keeping track of the SARS-CoV-2 vaccine pipeline. Nat. Rev. Immunol. *20*, 650. https://doi.org/10.1038/s41577-020-00455-1.

Pépin, G., Nejad, C., Thomas, B.J., Ferrand, J., McArthur, K., Bardin, P.G., Williams, B.R., and Gantier, M.P. (2017). Activation of cGAS-dependent antiviral responses by DNA intercalating agents. Nucleic Acids Res. *45*, 198–205. https://doi.org/10.1093/nar/gkw878.

Persinoti, G.F., de Aguiar Peres, N.T., Jacob, T.R., Rossi, A., Vêncio, R.Z., and Martinez-Rossi, N.M. (2014). RNA-sequencing analysis of Trichophyton rubrum transcriptome in response to sublethal doses of acriflavine. BMC Genomics *15*, S1. https://doi.org/10.1186/1471-2164-15-s7-s1.

Pervushin, K., Riek, R., Wider, G., and Wüthrich, K. (1997). Attenuated T2 relaxation by mutual cancellation of dipole-dipole coupling and chemical shift anisotropy indicates an avenue to NMR structures of very large biological macromolecules in solution. Proc. Natl. Acad. Sci. U S A *94*, 12366–12371. https://doi.org/10.1073/pnas.94.23.12366.

Ratia, K., Saikatendu, K.S., Santarsiero, B.D., Barretto, N., Baker, S.C., Stevens, R.C., and Mesecar, A.D. (2006). Severe acute respiratory syndrome coronavirus papain-like protease: structure of a viral deubiquitinating enzyme. Proc. Natl. Acad. Sci. U S A *103*, 5717–5722. https://doi.org/10.1073/pnas.0510851103.

Reed, L.J., and Muench, H. (1938). A simple method of estimating fifty per cent endpoints12. Am. J. Epidemiol. *27*, 493–497. https://doi.org/10.1093/oxfordjournals.aje.a118408.

Rees, R.W., Brice, A.J., Carlton, J.B., Gilbert, P.J., and Mitchell, I.D. (1989). Optimization of metabolic activation for four mutagens in a bacterial, fungal and two mammalian cell mutagenesis assays. Mutagenesis *4*, 335–342. https://doi.org/10.1093/mutage/4.5.335.

Robert, X., and Gouet, P. (2014). Deciphering key features in protein structures with the new ENDscript server. Nucleic Acids Res. *42*, W320–W324. https://doi.org/10.1093/nar/gku316.

Saha, R.P., Sharma, A.R., Singh, M.K., Samanta, S., Bhakta, S., Mandal, S., Bhattacharya, M., Lee, S.S., and Chakraborty, C. (2020). Repurposing drugs, ongoing vaccine, and new therapeutic development initiatives against COVID-19. Front Pharmacol. *11*, 1258. https://doi.org/10.3389/fphar.2020.01258.

Schneider, C.A., Rasband, W.S., and Eliceiri, K.W. (2012). NIH Image to ImageJ: 25 years of image analysis. Nat. Methods *9*, 671–675. https://doi.org/10.1038/nmeth.2089.

Shamsi, A., Mohammad, T., Anwar, S., Amani, S., Khan, M.S., Husain, F.M., Rehman, M.T., Islam, A., and Hassan, M.I. (2021). Potential drug targets of SARS-CoV-2: from genomics to therapeutics. Int. J. Biol. Macromol *177*, 1–9. https://doi.org/10.1016/j.ijbiomac.2021.02.071.

Shin, D., Mukherjee, R., Grewe, D., Bojkova, D., Baek, K., Bhattacharya, A., Schulz, L., Widera, M., Mehdipour, A.R., Tascher, G., et al. (2020). Papain-like protease regulates SARS-CoV-2 viral spread and innate immunity. Nature *587*, 657–662. https://doi.org/10.1038/s41586-020-2601-5.

Shin, D.H., Choi, K.S., Cho, B.S., Song, S., Moon, D.C., Hong, J.T., Lee, C.K., and Chung, Y.B. (2008). Pharmacokinetics of guanosine in rats following intravenous or intramuscular administration of a 1:1 mixture of guanosine and acriflavine, a potential antitumor agent. Arch. Pharm. Res. *31*, 1347–1353. https://doi.org/10.1007/s12272-001-2116-z.

Simonovich, V.A., Burgos Pratx, L.D., Scibona, P., Beruto, M.V., Vallone, M.G., Vázquez, C., Savoy, N., Giunta, D.H., Pérez, L.G., Sánchez, M.D.L., et al. (2020). A randomized trial of convalescent plasma in covid-19 severe pneumonia. N. Engl. J. Med. https://doi.org/10.1056/NEJMoa2031304.

Song, S., Kwon, O.S., and Chung, Y.B. (2005). Pharmacokinetics and metabolism of acriflavine in rats following intravenous or intramuscular administration of AG60, a mixture of acriflavine and guanosine, a potential antitumour agent. Xenobiotica *35*, 755–773. https://doi.org/10.1080/00498250500188073.

Tickle, I.J., Flensburg, C., Keller, P., Paciorek, W., Sharff, A., Vonrhein, C., and Bricogne, G. (2018). STARANISO (Global Phasing Ltd.).

Tripathi, R.P., Verma, S.S., Pandey, J., Agarwal, K.C., Chaturvedi, V., Manju, Y.K., Srivastva, A.K., Gaikwad, A., and Sinha, S. (2006). Search of antitubercular activities in tetrahydroacridines: synthesis and biological evaluation. Bioorg. Med. Chem. Lett. *16*, 5144–5147. https://doi.org/10.1016/j.bmcl.2006.07.025.

van der Hoek, L., Pyrc, K., Jebbink, M.F., Vermeulen-Oost, W., Berkhout, R.J., Wolthers, K.C., Wertheim-van Dillen, P.M., Kaandorp, J., Spaargaren, J., and Berkhout, B. (2004). Identification of a new human coronavirus. Nat. Med. *10*, 368–373. https://doi.org/10.1038/nm1024.

Verma, M., Choi, J., Cottrell, K.A., Lavagnino, Z., Thomas, E.N., Pavlovic-Djuranovic, S., Szczesny, P., Piston, D.W., Zaher, H.S., Puglisi, J.D., and Djuranovic, S. (2019). A short translational ramp determines the efficiency of protein synthesis. Nat. Commun. *10*, 5774. https://doi.org/10.1038/s41467-019-13810-1.

Villarroya-Beltri, C., Guerra, S., and Sánchez-Madrid, F. (2017). ISGylation - a key to lock the cell gates for preventing the spread of threats. J. Cell Sci *130*, 2961–2969. https://doi.org/10.1242/jcs.205468.

Wainwright, M. (2001). Acridine-a neglected antibacterial chromophore. J. Antimicrob. Chemother. *47*, 1–13. https://doi.org/10.1093/jac/47.1.1.

Yang, H., Xie, W., Xue, X., Yang, K., Ma, J., Liang, W., Zhao, Q., Zhou, Z., Pei, D., Ziebuhr, J., et al. (2005). Design of wide-spectrum inhibitors targeting coronavirus main proteases. PLoS Biol. *3*, e324. https://doi.org/10.1371/journal.pbio.0030324.

Zaki, A.M., van Boheemen, S., Bestebroer, T.M., Osterhaus, A.D., and Fouchier, R.A. (2012). Isolation of a novel coronavirus from a man with pneumonia in Saudi Arabia. N. Engl. J. Med. *367*, 1814–1820. https://doi.org/10.1056/NEJMoa1211721.

Zhang, Y., Werling, U., and Edelmann, W. (2014). Seamless ligation cloning extract (SLiCE) cloning method. Methods Mol. Biol. *1116*, 235–244. https://doi.org/10.1007/978-1-62703-764-8_16.

STAR★METHODS

KEY RESOURCES TABLE

REAGENT or RESOURCE	SOURCE	IDENTIFIER
Antibodies		
Mouse monoclonal anti-SARS-CoV-2 nucleocapsid protein	Bioss Antibodies	Cat# bsm-41412M
Goat polyclonal anti-mouse IgG (H + L) conjugated with Alexa Fluor 546	Invitrogen	Cat# A-11003; RRID: AB_2534071
Anti-Ubiquitin antibody	Santa-Cruz	Cat# Sc-8017; RRID: AB_628423
Donkey anti-mouse IgG (H + L)-HRPO	Dianova	Cat# 715-035-150; RRID: AB_2340770
Bacterial and virus strains		
E. coli strain BL21 (DE3)	Thermo Fisher	EC0114
SARS-CoV-2 strain: BavPat1/2020	EVAg	Ref-SKU: 026V-03883
MERS-CoV isolate England 1	National Collection of Pathogenic Viruses	1409231v
FIPV strain 79-1146	Kindly granted by Gergely Tekes, Justus Liebig University Giessen, Germany	N/A
HCoV-NL63 isolate Amsterdam 1	(van der Hoek et al., 2004)	GenBank: AY567487.2
HCoV-OC43	ATCC	VR-1558
Biological samples		
Human airway epithelial (HAE) cells	Silesian Centre for Heart Diseases, Medical University of Silesia in Katowice	N/A
MucilAir™-Bronchial HAE	Epithelix Sarl	EP01MD
Chemicals, peptides, and recombinant proteins		
Acriflavine (ACF)	Sigma-Aldrich	Cat# A8251
Remdesivir (REM)	Gilead Sciences	N/A
Verteporfin	Sigma-Aldrich	Cat# SML0534
Evans Blue	Sigma-Aldrich	Cat# E2129
Clofazimine	Sigma-Aldrich	Cat# C8895
Hypericin from *Hypericus perforatum*	Sigma-Aldrich	Cat# 00190585
Dithranol	Sigma-Aldrich	Cat# D2773
Chlorophyllin sodium copper salt	Sigma-Aldrich	Cat# C6003
Acriflavine hydrochloride	Sigma-Aldrich	Cat# A8251
Protoporphyrin IX	Sigma-Aldrich	Cat# P8293
Tannic acid	Sigma-Aldrich	Cat# 403040
PHA-665752 hydrate	Sigma-Aldrich	Cat# PZ0147
Proflavine hemisulfate salt hydrate	Sigma-Aldrich	Cat# P2508
Paraformaldehyde (PFA)	Sigma-Aldrich	Cat# P6148-1KG
TEV	EURx	E4310-02
IPTG	Lab Empire	IPT001.1
ISG15-AMC	Boston Biochem	Cat# UL-553
Z-Arg-Leu-Arg-Gly-Gly-AMC	Enzo lifesciences	BML-ZW8585-0005
Tri-Ubiquitin/Ub3 WT Chains (K48-linked)	Boston Biochem	Cat# UC-215B
Critical commercial assays		
XTT Cell Viability Assay kit	Biological Industries	SKU: 20-300-1000
Viral DNA/RNA kit	A&A Biotechnology	Cat# 034-100
mirVanaTM miRNA Isolation kit	Thermo Fisher	Cat# AM1560
Crystallization kit	Natrix HT	Cat# HR2-131
GoTaq Probe 1-Step RT-qPCR System	Promega	Cat# A6121

(*Continued on next page*)

Continued

REAGENT or RESOURCE	SOURCE	IDENTIFIER
Deposited data		
PL^{pro} – ACF structure	This paper; Protein Data Bank	PDB: 7NT4
PL^{pro} (apo) structure	Protein Data Bank	PDB: 6W9C
Experimental models: Cell lines		
Vero	ATCC	CCL-81
HCT-8	ATCC	CCL-244
CRFK	ATCC	CCL-94
$A549^{ACE2+}$	(Milewska et al., 2014)	N/A
LLC-MK2	ATCC	CCL-7
Primary human skin fibroblasts (HSF)	Sigma	C0135C
Experimental models: Organisms/strains		
K18-hACE2 transgenic mouse	The Jackson Laboratory	Stock no.: 034860
Oligonucleotides		
Primers for a RT-qPCR, see Table S2	This paper	N/A
Recombinant DNA		
Plasmid: pETDuet-1	Merck Millipore	71146-3
Plasmid: pETM11	G.Stier-EMBL	N/A
Plasmid: pETM13	G.Stier-EMBL	N/A
Plasmid: pETM5a	This paper	N/A
Plasmid: PLPro construct comprising amino acids 1564-1878 of SARS-CoV-2	IDT	N/A
Plasmid: Mpro construct comprising amino acids 3264-3569 of SARS-CoV-2	GeneArt	N/A
Software and algorithms		
Graph Pad Prism 8 software	Graph Pad Prism	https://www.graphpad.com/scientific-software/prism/
ImageJ	(Schneider et al., 2012)	https://imagej.nih.gov/ij/
MEGA X	(Kumar et al., 2018)	https://www.megasoftware.net/
Pymol	Pymol by Schroedinger	https://pymol.org/2/
XDS software	(Kabsch, 2010)	https://xds.mr.mpg.de/
STARANISO web server	(Tickle et al., 2018)	https://staraniso.globalphasing.org/cgi-bin/staraniso.cgi
Other		
Fetal bovine serum heat-inactivated (FBS HI)	Thermo Fisher	Cat# 10500064
Dulbecco’s MEM	Corning	Cat# 10-017-CV
Penicillin-Streptomycin	PAN-Biotech	Cat# P06-07100
Ciprofloxacin	Fluka	Cat# 17850-5G-F
G-418	Roche/Merck	Cat# 108321-42-2
Hanks’ MEM	Thermo Fisher	Cat# 21575-022
Earle’s MEM	Thermo Fisher	Cat# 31150-022
MEM Non-Essential Amino Acids Solution	Thermo Fisher	Cat# 11140050
MucilAir^{TM} culture medium	Epithelix Sarl	Cat# EP04MM
PBS	Thermo Fisher	Cat# 70011044
DAPI	Sigma-Aldrich	Cat# D9542-5MG
Alexa Fluor 647 Phalloidin	Thermo Fisher	Cat# A22287
ProLong™ Diamond Antifade Mountant	Thermo Fisher	Cat# P36961
Thincert cell culture insert for 12 well plates	Greiner Bio-One	Item No.: 665641
Terrific Broth (TB)	Merck Millipore	T0918-1KG
Ni-NTA Agarose	Jena Bioscience	AC-501-25

(*Continued on next page*)

Continued

REAGENT or RESOURCE	SOURCE	IDENTIFIER
HiLoad 16/600 Superdex 75 pg	Cytiva (GE Healthcare Life Sciences)	28989333
Invitrogen NuPAGE^{TM} 4–12% Bis-Tris	Thermo Fisher	NP0322BOX

RESOURCE AVAILABILITY

Lead contact

Further information and requests for resources and reagents should be directed to and will be fulfilled by the lead contact, Krzysztof Pyrc (k.a.pyrc@uj.edu.pl).

Materials availability

This study generated a new expression vector, pETM5a.

Data and code availability

All data reported in this paper will be shared by the lead contact upon request.

This paper does not report original code.

Any additional information required to reanalyze the data reported in this paper is available from the lead contact upon request.

EXPERIMENTAL MODEL AND SUBJECT DETAILS

Animal studies

8–10-week-old female transgenic mice expressing the human ACE2 protein under the human cytokeratin 18 promoter (K18-hACE2) were purchased from the Jackson Laboratory (Bar Harbor, ME, USA). Mice were maintained in individually ventilated cages, on a 12/12-hour light/dark cycle, with the RT maintained at 22° ± 1 and fed a standard laboratory diet and water ad libitum under SPF conditions within the ABSL-3 facility at Malopolska Centre of Biotechnology, Jagiellonian University, Krakow, Poland. Mice were randomly assigned to experimental groups. Control and virus-infected mice were housed in separate cages. Mice were quarantined for at least 7 days prior to the experiment. All animal studies were performed in accordance with the protocols laid down by the Institutional Animal Care and Use II Regional Ethics Committee on Animal Experimentation, Krakow, Poland (approval no. 150/2021).

Cells

Vero (*Cercopithecus aethiops*; kidney epithelial; ATCC CCL-81), HCT-8 (ATCC CCL-244) cells, derivative of HRT-18 (*Homo sapiens*; male; ileocecal colorectal adenocarcinoma; ATCC CCL-244), CRFK (*Felis catus;* female; kidney cortex; ATCC CCL-94) were cultured in Dulbecco's MEM (Corning, Poland) supplemented with 5% fetal bovine serum (heat-inactivated FBS HI; Thermo Fisher Scientific, Poland) and antibiotics: penicillin-streptomycin (10 U/ml penicillin and 100 μg/ml streptomycin; PAN-Biotech, Germany), and ciprofloxacin (5 μg/ml, Fluka). A549 (*Homo Sapiens; male;* lung carcinoma cells, ATCC CCL-185)cells with ACE2 overexpression (A549^{ACE2+}) (Milewska et al., 2014) were cultured in the same manner but supplemented with G418 (5 mg/ml; Roche/Merck, Germany, Canada).

LLC-MK2 cells (; Macaca mulatta kidney epithelial cells; ATCC CCL-7) were maintained in minimal essential medium (MEM; two parts Hanks' MEM and one part Earle's MEM (Thermo Fisher, Poland]) 5% FBS HI, penicillin-streptomycin (10 U/ml penicillin and 100 μg/ml streptomycin, and ciprofloxacin (5 μg/ml).

Primary human skin fibroblasts (HSF; male; in house isolation) were cultured in Dulbecco's MEM (Thermo Fisher Scientific, Poland) supplemented with 10% FBS 1% nonessential amino acids (Thermo Fisher, Poland) and antibiotics: penicillin-streptomycin (10 U/ml penicillin and 100 μg/ml streptomycin, and ciprofloxacin (5 μg/ml).

Human airway epithelial (HAE) cells were isolated from conductive airways resected from transplant patients. The study was approved by the Bioethical Committee of the Medical University of Silesia in Katowice, Poland (approval no: KNW/0022/KB1/17/10 dated 16.02.2010). Written consent was obtained from all patients. Cells were dislodged by protease treatment and later mechanically detached from the connective tissue. Further, cells were trypsinized and transferred onto permeable Transwell insert supports (φ = 6.5 mm). Cell differentiation was stimulated by the media additives and removal of media from the apical side after the cells reached confluence. Finally, cells were cultured for 4-6 weeks to form well-differentiated, pseudostratified mucociliary epithelium. All experiments were performed in accordance with relevant guidelines and regulations. Commercially available MucilAir™-Bronchial (Epithelix Sarl, Switzerland) HAE cultures were also used for the *ex vivo* analysis. MucilAir™ cultures were maintained as suggested by the provider in MucilAir™ culture medium. All cells were maintained at 37°C under 5% CO_2.

Viruses

Reference SARS-CoV-2 strain 026V-03883 was kindly granted by Christian Drosten, Charité – Universitätsmedizin Berlin, Germany by the European Virus Archive - Global (EVAg); https://www.european-virus-archive.com/).

All SARS-CoV-2 stocks were generated by infecting monolayers of Vero cells. The cells were incubated at 37 °C under 5% CO_2. The virus-containing liquid was collected at day 2 post-infection (p.i.), aliquoted, and stored at −80°C. Control samples from mock-infected cells were prepared in the same manner.

MERS-CoV stock (isolate England 1, 1409231v, National Collection of Pathogenic Viruses, Public Health England, United Kingdom) was generated by infecting monolayers of Vero cells. The cells were incubated at 37°C under 5% CO_2. The virus-containing liquid was collected at day 3 p.i., aliquoted, and stored at −80°C. Control samples from mock-infected cells were prepared in the same manner.

FIPV stock (strain 79-1146) was generated by infecting CRFK cells at 90% confluency. The cells were incubated at 37 °C under 5% CO_2. The virus-containing liquid was collected at day 3 p.i., aliquoted, and stored at −80°C. Control samples from mock-infected cells were prepared in the same manner.

The HCoV-NL63 stock (isolate Amsterdam 1) was generated by infecting monolayers of LLC-MK2 cells. The cells were incubated at 32°C under 5% CO_2 and then lysed by two freeze-thaw cycles at 6 days p.i. The virus-containing liquid was aliquoted and stored at −80°C. A control LLC-MK2 cell lysate from mock-infected cells was prepared in the same manner.

The HCoV-OC43 stock (ATCC: VR-1558) was generated by infecting monolayers of HRT-18 cells. The cells were incubated at 32°C under 5% CO_2 and then lysed by two freeze-thaw cycles at 5 days post-infection (p.i.). The virus-containing liquid was aliquoted and stored at −80°C. A control HRT-18G cell lysate from mock-infected cells was prepared in the same manner.

Virus yields were assessed by titration on fully confluent cells in 96-well plates, according to the method of Reed and Muench (1938). Plates were incubated at 32°C or 37°C, and the cytopathic effect (CPE) was scored by observation under an inverted microscope.

METHOD DETAILS

Plasmids and proteins

Gene encoding the PL^{pro} (SARS-CoV-2 nsp3 - 1564-1878) was synthesized by Integrated DNA Technologies (IDT-Coralville, USA) optimized for *E. coli* expression and cloned using the Slice method (Zhang et al., 2014) into several vectors, including pETM11, pETM13 with a C-terminal His_6 and a new expression vector named petM5a, a modified pETM11 vector. The pETM5a vector contains an insertion of optimized codon sequence after the starting codon ATG, GTG AAG TAT CAA AAG, based on Verma et al. (2019), and followed by the N- terminal His_6 tag, and by a TEV protease site. The vector map can be found at HMGU-PEPF website. The plasmids were transformed into *E. coli* BL21 (DE3), and the transformed cells were cultured at 37°C in terrific broth (TB) media containing 100 mg/l kanamycin. After the OD_{600} reached 2, the culture was cooled to 18°C and supplemented with 0.25 mM IPTG. The vector petM5a yielded more soluble protein and was used for all protein expression. For isotopically labeled protein, pre-culture was grown in M9 minimal media followed by inoculation (OD_{600} 0.05) into 1 l of D_2O M9 minimal media supplemented with ^{15}N-ammoniun chloride. After OD_{600} reached 0.8, the culture was cooled to 18°C and supplemented with 0.25 mM IPTG. After overnight induction, the cells were harvested by centrifugation, and the pellets were resuspended in lysis buffer (20 mM Tris-HCl, pH 8.5, 350 mM NaCl, 10% glycerol, 10 mM imidazole, 5 mM beta-mercaptoethanol) and sonicated at 4°C. The insoluble material was removed by centrifugation at 24,000 rpm. The fusion protein was first purified by Ni-NTA affinity chromatography, the supernatant was applied to nickel resin and washed with 10 times the column volume of lysis buffer followed by a wash step of lysis buffer supplemented with 20 mM imidazole. The protein was eluted with 3 column volumes of a buffer containing high imidazole concentration (20 mM Tris-HCl, pH 8.5, 350 mM NaCl, 5% glycerol, 350 mM imidazole, 5 mM beta-mercaptoethanol). 1 mg of TEV protease was added, and the solution was dialyzed overnight at 4°C against a buffer containing low imidazole concentration, 20 mM Tris-HCl, pH 8.5, 150 mM NaCl, 5% glycerol, 10 mM imidazole, 1 mM beta mercaptoethanol. For the final step, the protein was applied to a size exclusion chromatography column, High load S75 (GE- Healthcare, Chicago, USA), pre-equilibrated with the final buffer, 20 mM Tris pH 8.0, 40 mM NaCl and 2 mM DTT. The purity of the protein was accessed by SDS-PAGE gel.

M^{pro} construct comprising amino acids 3264-3569 of SARS-CoV-2 polyprotein 1ab, N-terminal 6xHis and TEV protease cleavage site optimized for expression in *E. coli* was synthesized by GeneArt and subcloned into expression plasmid pETDuet-1. Protein expression was carried out in *E. coli* strain BL21 in TB media. After reaching OD_{600} = 1.2 the bacteria were induced by adding 0.5 mM IPTG, cultured for 3 h at 37°C, and harvested by centrifugation. Cells were then resuspended in a lysis buffer containing 50 mM Tris pH 8.5, 300 mM NaCl, 5% glycerol, 1% Triton X-100, 2 mM β-mercaptoethanol, and protease inhibitor cocktail and disintegrated by sonication. The lysate was cleared by centrifugation, filtered through a 0.45 μm filter and the protein was purified by nickel affinity (Ni-NTA Agarose, Jena Bioscience). TEV cleavage was carried out overnight in 50mM Tris pH 8.5, 250 mM NaCl, 5% glycerol and 4 mM β-mercaptoethanol. TEV and uncut M^{pro} were removed by a second NiNTA purification step. The protein was further purified by size exclusion chromatography (Superdex s75, GE Healthcare) in 50mM Tris pH 7.4, 150mM NaCl, 2mM β-mercaptoethanol.

PL^{pro} activity assay

The assay was designed to measure PL^{pro} protease activity under screening conditions in white 384-well Optiplates. The assay buffer contained 50 mM Tris-HCl (pH 8.0), 0.01% (w/v) BSA and 10 mM DTT. RLRGG-AMC was used as a fluorogenic substrate for PL^{pro}

40 μl of PL^{pro} protein (final concentration 60 nM) was incubated with 10 μl RLRGG-AMC substrate (final concentration 400 nM). The mixture (final volume 50 μl) was incubated for 30 min. The release of AMC (λ_{ex} = 360 nm; λ_{em} = 487 nm) was measured on an Envision plate reader (Perkin Elmer, Waltham, MA).

M^{pro} activity assay

The main protease activity assay was adapted from previously described kinetic assays (Yang et al., 2005). The cleavage of the fluorogenic substrate MCA-AVLQSGFR-Lys(Dnp)-Lys-NH2 (Peptide Specialty Laboratories, Heidelberg) was monitored over 30 min using a microplate reader (PerkinElmer) with excitation and emission wavelengths of 320 nm and 405 nm, respectively. Different concentrations of acriflavine were incubated with 2 μM main protease before the reaction was initiated by the addition of fluorogenic substrate. The measurement was performed in Greiner black flat bottom 384-well microplates. The final reaction volume of 50 μl contained 2 μM main protease, 15 μM fluorogenic substrate and acriflavine in a buffer consisting of 50 mM Tris-HCl (pH 7.3), 150mM NaCl, 1 mM EDTA and 1% DMSO.

Compound screening

40 μl of PL^{pro} protein (final concentration 60nM) in assay buffer (50 mM Tris-HCl (pH 8.0), 0.01% (w/v) BSA, and 10 mM DTT) was added to the screening plates using the MultiFlo dispensing system (BioTek). Compounds and DMSO (control sample) were directly pipetted into the screening plates to achieve a final concentration of 10 μM using a Sciclone G3 liquid handling workstation (PerkinElmer, Waltham, USA). The drug repurposing collection (Corsello et al., 2017) was used to identify PL^{pro} inhibitors. The controls in the plates (first two and last two columns) included DMSO control (negative control with no compound) and control without protein (to obtain the assay window). After addition of 10 μl RLRGG-AMC substrate (final concentration 400 nM) with the MultiFlo, AMC fluorescence (λ_{ex} = 360 nm; λ_{em} = 487 nm) was measured using a Envision plate reader immediately after substrate addition (time point 0) and after 30 min (time point 1). The average Z′ factor for all plates was above 0.8, showing excellent screening quality. As a cut-off value for active compounds, we choose 4x the standard deviation below median of all compound-treated wells (calculated per plate). after removing compounds that generated high fluorescence signal at time point 0 (suggesting unspecific compound interference).

We also assessed PL^{pro} inhibition with ACF and two derivatives of ACF, namely acridine orange base and acridine-3,6-diamine sulfate (Figure S1D), as well as the previously published PL^{pro} inhibitor GRL-0167 (Shin et al., 2020) (Figure S1E). All derivatives showed dose-dependent inhibition of PL^{pro}, but were less active than the parent compound.

PL^{pro} inhibitor IC$_{50}$ determination

RLRGG-AMC or ISG15-AMC were used as substrates for PL^{pro,} and the release of AMC fluorescence was measured (λ_{ex} = 360 nm; λ_{em} = 487 nm) on an Envision plate reader. 40 μl of a 75 nM PL^{pro} solution in assay buffer (50 mM Tris-HCl (pH 8.0), 0.01% (w/v) BSA and 10 mM DTT) was pipetted into 384 well plates and different concentrations of ACF (50 μM–0 μM, final concentration). Note that the DMSO concentration was kept constant in all reactions. The mixture was incubated for 1 h at RT. Then the reaction was initiated by adding 10 μl of 2 μM RLRGG-AMC (final concentration 400 nM) or 10 μl of 0.5 μM ISG15-AMC (final concentration 100 nM), respectively. Initial velocities of AMC release were normalized to the DMSO control. The IC$_{50}$ value was calculated using GraphPad Prism. The experiment was repeated three times.

Gel-based PL^{pro} DUB activity

0.2 μM PL^{pro} was preincubated with 0, 10, 30 or 50 μM ACF for 30 min in 20 μl reaction buffer (20 mM Tris-HCl pH 7.5, 100 mM NaCl, 10 mM DTT) at 23°C. Note that the DMSO concentration was kept constant in all reactions. In the next step 20 μl of 4 μM tri-ubiquitin K48-linked (Boston Biochem) diluted in the reaction buffer was added to the pre-mix. Final enzyme and substrate concentrations were 0.1 μM and 2 μM, respectively. At indicated time points, the reaction was stopped by mixing 5 μl of the reaction with 15 μl 4x concentrated gel-loading buffer (Carl Roth), and the samples were analyzed by SDS–PAGE (Invitrogen NuPAGE^{TM} 4–12% Bis-Tris) and western blot (anti-ubiquitin, P4D1, Santa Cruz Biotechnology).

Chemical characterization of the ACF components

The commercial ACF (Sigma-Aldrich/Merck #A8251) is sold as a mixture of 3,6-diaminoadridin-10-ium (proflavine) and 3,6-diamino-10-methylacridin-10-ium (acriflavine). In order to perform the study using fully characterized material, we have used NMR and HPLC/MS techniques to analyze the commercial product. The analysis revealed 56% proflavine (**PF**), 17% acriflavine (**ACF**), and 22–23% side methylated **PF**. The remaining 4–5% are other 3,6-diaminoacridine derivatives like for example, side methylated **ACF** (4%) (See supplementary analysis).

Cell viability assay

Cell viability was evaluated using the XTT Cell Viability Assay kit (Biological Industries, Cromwell, CT, USA) according to the manufacturer's protocol. Vero, A549^{ACE2+}, CRFK, HRT-18, LLC-MK2, and HSF cells were cultured on 96-well plates. Cells were incubated with ACF for 24 h at 37°C in an atmosphere containing 5% CO$_2$. After incubation, the medium was discarded and 100 μL of fresh medium was added to each well. Then, 25 μL of the activated 2,3-bis-(2-methoxy-4-nitro-5-sulphenyl)-(2H)-tetrazolium-5-carboxanilide (XTT) solution was added and samples were incubated for 2 h at 37°C. The absorbance (λ = 450 nm) was measured using a

Spectra MAX 250 spectrophotometer (Molecular Devices, San Jose, CA, USA). The obtained results were normalized to the control samples, where cell viability was set to 100%.

Isolation of nucleic acids, RT-qPCR

A viral DNA/RNA kit (A&A Biotechnology, Poland) was used for nucleic acid isolation from cell culture supernatants. RNA was isolated according to the manufacturer's instructions.

Viral RNA was quantified using quantitative PCR coupled with reverse transcription (RT-qPCR) (GoTaq Probe 1-Step RT-qPCR System, Promega, Poland) using CFX96 Touch Real-Time PCR detection system (Bio-Rad, Poland). The reaction was carried out in the presence of the probes and primers indicated in Table S2. The heating scheme was as follows: 15 min at 45°C and 2 min at 95°C, followed by 40 cycles of 15 s at 95°C and 1 min at 58°C or 60°C. In order to assess the copy number of the N gene, standards were prepared and serially diluted.

Virus replication inhibition assay

Vero cells were seeded in culture medium on 96-well plates (TPP, Trasadingen, Switzerland) at 2 days before infection. Subconfluent cells were infected with SARS-CoV-2 viruses at 1600 50% tissue culture infectious dose ($TCID_{50}$)/ml. Infection was performed in the presence of 100 nM, 1 μM, and 10 μM concentrations of compounds listed in Table S1. After 2 h of incubation at 37°C, cells were rinsed twice with PBS, and a fresh medium with compounds was added. The infection was carried out for 48 h, and the cytopathic effect (CPE) was assessed. Culture supernatants were collected from wells where CPE reduction was observed.

For the detailed determination of the antiviral properties of ACF, susceptible cells were seeded in a culture medium on 96-well plates at 2 days before infection. Subconfluent cells were infected with SARS-CoV-2, MERS-CoV and FIPV viruses at $TCID_{50}$ = 1600 and HCoV-NL63 at $TCID_{50}$ = 4000 and HCoV-OC43 at $TCID_{50}$ = 3000. Infection was performed in the presence of ACF. Control cells were inoculated with the same volume of mock as a negative control and with 10 μM remdesivir (REM) as a positive control of coronavirus replication inhibition. After 2 h of incubation at 37°C, cells were rinsed twice with PBS, and fresh medium without or with ACF or remdesivir was added. The infection was carried out for 24 h when the CPE in virus control was observed. Culture supernatants and cell lysates were collected for the RT-qPCR analysis. To obtain the latter ones, cells were lysed with 100 μl of R9F lysis buffer from the viral RNA isolation kit (A&A Biotechnology, Poland) for 5 minutes at RT. Supernatants for the plaque assay were collected 48 h p.i.

Virus replication inhibition *ex vivo* was evaluated by infecting HAE cultures with SARS-CoV-2 virus at 5000 $TCID_{50}$/ml in the presence of ACF, remdesivir or PBS. Two concentrations of ACF (400 nM and 500 nM) and the controls were added to the apical side of the inserts, followed by the addition of the virus diluted in PBS. Infection time was 2 hours at 32°C or 37°C. After the infection, the apical side of the HAEs were washed three times with PBS, and each compound was re-applied and incubated again for 30 minutes at 37°C. After the last incubation with the ACF, the samples (50 μl) were collected, and the HAEs were left in air-liquid interphase. Every 24 hours, the HAEs were incubated for 30 minutes with the ACF dilutions or controls, and the samples were collected. After collecting the last samples, cells were fixed with 3.7% paraformaldehyde (Sigma-Aldrich, Poland) and stained as described below. Virus yield was measured using the RT-qPCR method described below.

Plaque assay

Vero E6 cells were seeded in 24 well plates 24 h prior to the inoculation. At the day of infection, 80–90% confluent cells were overlaid with 200 μl of 10-fold serial dilutions of samples. Following 1 h incubation at 37°C, cells were overlaid with 1 ml of DMEM media supplemented with 10% heat-inactivated FBS, penicillin/streptomycin and 1% methylcellulose (Sigma-Aldrich, Poland). 72 h p.i. cells were fixed for at least 4 h with 4% PFA, the buffer was discarded, and cells were stained using 0.1% crystal violet solution in 50:50 water/methanol solution for 10 min at room temperature. Finally, cells were washed with water and plaques were counted. All samples for a plaque assay were collected from at least three experiments each in triplicate and every sample was overlaid in duplicate. The titer of samples was calculated by following formulas:

$$TCID_{50} = \text{titer}\left(\frac{pfu}{ml}\right) \Big/ 0.69$$

$$titer\left(\frac{pfu}{ml}\right) \times dilution\ factor \times \left(\frac{1}{ml\ of\ inoculum\ per\ well}\right)$$

Synergistic action of AFC and remdesivir

Synergistic effect of antiviral drugs was studied as reported previously, with some modifications (Benzekri et al., 2018). Virus replication assay was performed on confluent Vero cells. After 48 h the supernatants were collected, and virus yield was assessed by RT-qPCR as described above. The synergy was evaluated by calculating the combination index (CI) (Benzekri et al., 2018).

$$CI = \left(\frac{d1}{D1}\right) + \left(\frac{d2}{D2}\right)$$

where D1 and D2 are IC_{50} values (the doses required to reduce 50% of the viral infection) for remdesivir and the ACF, respectively. d1 is the dose of REM in presence of $IC_{50}/2$ of the active ACF required to reduce 50% of the viral infection, and d2 is the dose of the ACF in presence of $IC_{50}/2$ of remdesivir required to reduce 50% of the viral infection. D1, D2, d1 and d2 were determined by linear regression analysis from dose response curve. CI value ~1 indicates an additive effect, < 1 a synergistic effect, and > 1 an antagonistic effect.

Phylogenetic analysis

The evolutionary history was inferred by using the maximum likelihood method and the general time reversible model (Nei and Kumar, 2000). The tree with the highest log likelihood (−24114.75) is shown. Initial tree(s) for the heuristic search were obtained automatically by applying Neighbor-Join and BioNJ algorithms to a matrix of pairwise distances estimated using the maximum composite likelihood (MCL) approach and then selecting the topology with a superior log likelihood value. A discrete Gamma distribution was used to model evolutionary rate differences among sites (5 categories (+G, parameter = 2.6153)). The rate variation model allowed for some sites to be evolutionarily invariable ([+I], 4.79% sites). The tree is drawn to scale, with branch lengths measured in the number of substitutions per site. This analysis involved 17 nucleotide sequences. There were a total of 1576 positions in the final dataset. Evolutionary analyses were conducted in MEGA X (Kumar et al., 2018).

Virus visualization

$A549^{ACE2+}$ cells were seeded on coverslips in 12 well plates (TPP, Trasadingen, Switzerland) at 2 days before infection. Subconfluent cells were infected with SARS-CoV—2 in the presence of ACF or remdesivir. After 2 h infection, unbound virions were washed off twice with PBS, and fresh medium supplemented with compounds was added. The infection was carried out for 24 h, and 48 h whereupon cells were fixed with 3.7% paraformaldehyde (PFA) for 1 h. Fixed cells were permeabilized using 0.5% Tween 20 (10 min, room temperature [RT]), and unspecific binding sites were blocked with 5% bovine serum albumin (BSA) in PBS (4°C, overnight) prior to staining. For visualization of viral particles anti-SARS-CoV-2 nucleocapsid protein antibody (Bioss, bsm-41412M) at 1:200 dilution (2 h, RT) followed by Alexa Fluor 546 conjugated secondary antibody (Invitrogen, A-11003, 1:400 1 h, RT) was used. After incubating with antibodies, cells were washed thrice with 0.5% Tween-20. After labeling the virions, the actin cytoskeleton was visualized using Alexa-Fluor 647 conjugated phalloidin (4 U/mL, 1 h, RT, Thermo Scientific), and nuclear DNA was stained with 4′,6-diamidino-2-phenylindole (DAPI, 0.1 μg/ml, Sigma-Aldrich). Stained coverslips were mounted on glass slides with Prolong Diamond antifade mountant (Thermo Scientific, Poland). Fixed HAE cultures were permeabilized using 0.5% Triton X-100 (7 min RT), and unspecific binding sites were blocked with 5% BSA in PBS (1 h, 37°C) prior to staining. For visualization of virions anti-SARS-CoV-2 nucleocapsid protein antibody (Bioss bsm-41412M, 1:200 2 h, RT) coupled with goat anti-mouse Alexa Fluor 546 (Invitrogen, A-11003, 1:400 1 h, RT) were used. Nuclear DNA was stained with DAPI (0.1 μg/mL, 20 min, RT, Sigma-Aldrich) and actin cytoskeleton with Alexa Fluor 647 conjugated phalloidin (4 U/ml, 1 h, RT, Thermo Scientific). Stained HAE were cut from inserts and mounted on glass slides with cells facing coverslips. Fluorescent images were acquired under Zeiss LSM 880 confocal microscope.

Pharmacokinetics study of ACF in CD-1 mice

Pharmacokinetics study of ACF in mice was conducted at Enamine/Bienta (Kiev, Ukraine). Male CD-1 mice, divided in 4 groups (two different administration routes and 2 control groups), were used in the study. Pharmacokinetic data in plasma and lung samples were collected following intravenous (Iv) and peroral (Po) administration of commercial ACF at ten different time points. We have conducted the pharmacokinetic study at relatively high doses (15 and 100 mg/kg of ACF mixture containing all components, for intravenous and oral delivery respectively) due to separation and the detection limit of LC/MS specifically for the minor components of the mixture (NHMe-ACF content is only 4%). Also we expected high clearance from plasma. This might cause saturation of clearance mechanisms and a certain overestimation of the lung exposure. Plasma and lung samples were collected from mice and handled according to Enamine PK study protocols and the Institutional Animal Care and Use Guidelines. Concentrations of ACF, PF, side methylated ACF and side methylated PF were determined using high performance liquid chromatography/tandem mass spectrometry (HPLC-MS/MS). The concentration of the test compounds below the lower limits of quantification (LLOQ) were assigned as zero. Pharmacokinetics data were analyzed using noncompartmental, bolus injection or extravascular input models in WinNolin5.2 (PharSight).

Animal study

Transgenic mice expressing the human ACE2 protein under the human cytokeratin 18 promoter were purchased from the Jackson Laboratory. Mice were quarantined for at least 7 days prior to the experiment. Each experimental group consisted of 10 animals (14 animals in the control group). To take into account the fast metabolism of ACF, the compound was administered as a drinking solution (100 mg/kg body weight per day) and intramuscularly (5 mg/kg body weight or 15 mg/kg body weight twice a day). The treatment control group received remdesivir intramuscularly (25 mg/kg body weight per day). To mask the potentially unpleasant taste of the ACF that could lead to mice drinking less liquid than appropriate, all groups of mice were given sweetened isotonic drink instead of water. This is because, in our experience, the beverage is preferred by mice and well suited to dissolve the potentially unpleasant-tasting medications. The amount of drink consumed per day was determined prior to the experiment, and the concentration of ACF was adjusted to ensure the intended dose. Mice had free, permanent access to the drink during the experiment (from day −1 to 6 post-infection).

Mice treated intramuscularly received ACF every 12 hours as saline solution or remdesivir every 24 hours as a saline solution from day −1 until day 6 post-infection. No adverse effects were observed during the experiment.

On day 0 the animals were infected intranasally with the SARS-CoV-2 virus (Munchen-1.2 2020/984; 5 μl to each nostril) at 426,000 $TCID_{50}$/ml, which corresponded to ~3 × 10^5 pfu. The virus was propagated and titrated on Vero cells. Infected mice were examined and weighed daily. On day 6 post-infection, animals were sacrificed under anesthesia. Lungs and brains were collected. Tissues were homogenized using a bead homogenizer (TissueLyser II, Qiagen, Poland). Viral RNA was isolated using mirVana™ miRNA Isolation kit (ThermoFisher Scientific, Poland), and the viral infection was quantified using the RT-qPCR.

NMR spectroscopy

To assess the direct binding of ACF to PL^{pro} in a solution, we produced ^{15}N-labelled deuterated recombinant protein by growing the bacteria cultured in minimal M9 medium in D_2O. The protein purification is described earlier in the text. NMR experiments were recorded at 298 K on a Bruker Avance III 900 MHz spectrometer (^1H frequency 900 MHz) equipped with a 5 mm TCI cryoprobe. $^1H,^{15}N$ TROSY spectra (Nietlispach, 2005; Pervushin et al., 1997) were acquired with 40 scans and 1024 × 512 complex points on uniformly $^2H,^{15}N$-labelled PL^{pro} at 170 μM concentration in PBS buffer, pH 7.4 supplemented with 10% D_2O. Spectra were processed and analyzed using the AZARA suite of programs (v. 2.8, © 1993–2020; Wayne Boucher and Department of Biochemistry, University of Cambridge, unpublished). NMR titration experiments showed only localized alterations of spectra upon binding of ACF. No signs of oligomerization/aggregation were observed. This indicates that the third proflavine moiety observed in crystal structure at the interface between neighboring PL^{pro} molecules is indeed a crystallization artifact and that ACF does not cause dimerization of the PL^{pro} in solution. The multiple π-π stacked electron densities observed in the X-ray data between adjacent active sites also do not seem to cause PL^{pro} oligomerization as this would cause many resonances to shift upon the addition of a high concentration of ACF.

Crystallization and structure solution

PL^{pro} for crystallization was purified as described above. In the last step of purification, the protein was applied to size exclusion chromatography on S75 column using the following carrier buffer: 20 mM Tris-HCl pH 8.0, 40 mM NaCl, and 2 mM dithiothreitol (DTT). Purified protein was concentrated to 5–10 mg/ml using 30 kD cutoff Amicon Ultra Filter. The PL^{pro}-proflavine complex was prepared adding 5-fold molar excess of the compound to the concentrated protein. The final concentration of DMSO was kept below 5%. Crystallization samples were prepared using commercial kits and an automated crystallization workstation (Mosquito, TTP LabTech). Both ACF and pure proflavine were used in the experiments. Crystals of PL^{pro}-proflavine complex grew at room temperature in 0.05 M HEPES sodium salt pH 7, 0.05M magnesium sulfate, and 1.6 M lithium sulfate. Crystals suitable for testing were moved in cryo-protectant solution containing the harvesting solution supplemented with 25% (v/v) glycerol and snap-frozen in liquid nitrogen.

X-ray diffraction on PL^{pro}-proflavine crystals was determined at the Swiss Light Source (SLS, Villigen, Switzerland), beamline PXIII. The best dataset was collected at 2.7 Å resolution and it was indexed and integrated using XDS software (Kabsch, 2010); scaled and merged using STARANISO web server (Tickle et al., 2018). The crystal belongs to space group $P6_522$. Matthew's coefficient analysis suggested the presence of two PL^{pro}-proflavine molecules in the asymmetric unit. Molecular replacement solution was found using Phaser (McCoy, 2007; McCoy et al., 2007) and the apo PL^{pro} structure (PDB code: 6W9C) as a searching model. Model and restraints for proflavine were prepared using Lidia, the ligand builder in Coot (Emsley, 2017). The initial model was subjected to several iterations of manual and automated refinement cycles using COOT and REFMAC5, respectively (Emsley and Cowtan, 2004; Murshudov et al., 2011). Throughout the refinement, 5% of the reflections were used for cross-validation analysis (Brünger, 1992), and the behavior of R_{free} was employed to monitor the refinement strategy. Detailed information on data collection and refinement statistics is listed in Table S3. There are two molecules of the complex in the asymmetric unit. Intriguingly, a disulfide bond was found, which bridges two Cys270 of adjacent PL^{pro} molecules from different asymmetric units. An additional proflavine molecule is located at the interface between these symmetry mates between two molecules and is considered a crystallographic artifact (Figures S7A and S7B). The electron density analysis shows a weaker trace of at least two more proflavines that can be allocated on top of the other two at optimal distance for π-π staking forming a continuous, DNA-like stacking from one to another PL^{pro} molecule in the same asymmetric unit. Their electron density is much weaker and does not allow these molecules to be to built unambiguously (Figure S7C). However, they are not involved in any interaction with PL^{pro}.

QUANTIFICATION AND STATISTICAL ANALYSIS

Statistical analyses were performed using GraphPad Prism 8. All experiments were performed in triplicate, and results are presented as mean ± SEM unless otherwise indicated. One-way ANOVA with Tukey HSD post-hoc test was used to assess statistical significance of obtained results. When the parametric test assumptions were violated, the nonparametric Kruskal-Wallis with Dunn's post-hoc test was used. p values of 0.05 and less were considered significant.

Cell Chemical Biology, Volume *29*

Supplemental information

Acriflavine, a clinically approved drug,

inhibits SARS-CoV-2 and other betacoronaviruses

Valeria Napolitano, Agnieszka Dabrowska, Kenji Schorpp, André Mourão, Emilia Barreto-Duran, Malgorzata Benedyk, Pawel Botwina, Stefanie Brandner, Mark Bostock, Yuliya Chykunova, Anna Czarna, Grzegorz Dubin, Tony Fröhlich, Michael Hölscher, Malwina Jedrysik, Alex Matsuda, Katarzyna Owczarek, Magdalena Pachota, Oliver Plettenburg, Jan Potempa, Ina Rothenaigner, Florian Schlauderer, Klaudia Slysz, Artur Szczepanski, Kristin Greve-Isdahl Mohn, Bjorn Blomberg, Michael Sattler, Kamyar Hadian, Grzegorz Maria Popowicz, and Krzysztof Pyrc

SUPPLEMENTARY FIGURES

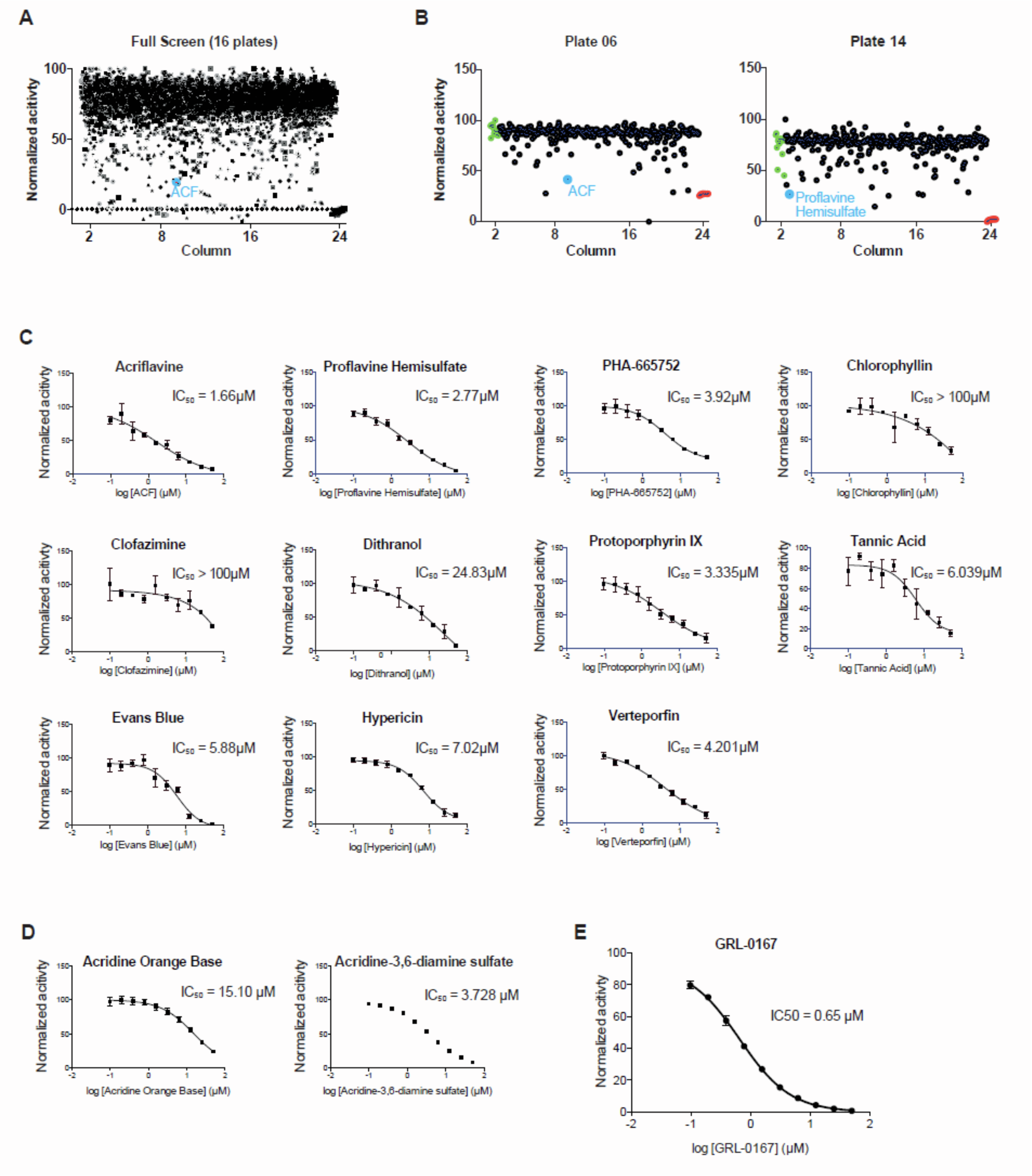

Figure S1. High-throughput screening, Related to Figure 1 (A) Summary of the high-throughput screening campaign (16 x 384-well plates). RLRGG-AMC peptide was used as a substrate for His-PL^{pro}. Each dot represents the data of one compound in one well (n = 1). Controls without protease are located in column 24, and ACF as a representative hit is depicted in blue. **(B)** Two representative screening plates with ACF and Proflavine Hemisulfate as hits (blue) are depicted side by side. **(C)** Dose-response curves of eleven hits. These hits were re-ordered and re-tested in ten-point titrations on the primary screening assay (mean ± SD, n = 2). Shown are inhibition curves and IC$_{50}$ values. **(D)** as in **(C)**. Analogs of ACF were tested in ten-point titrations on the primary assay (mean ± SD, n = 3). **(E)** Inhibition curve of the known PL^{pro} inhibitor GLR-0617 (mean ± SD, n = 3).

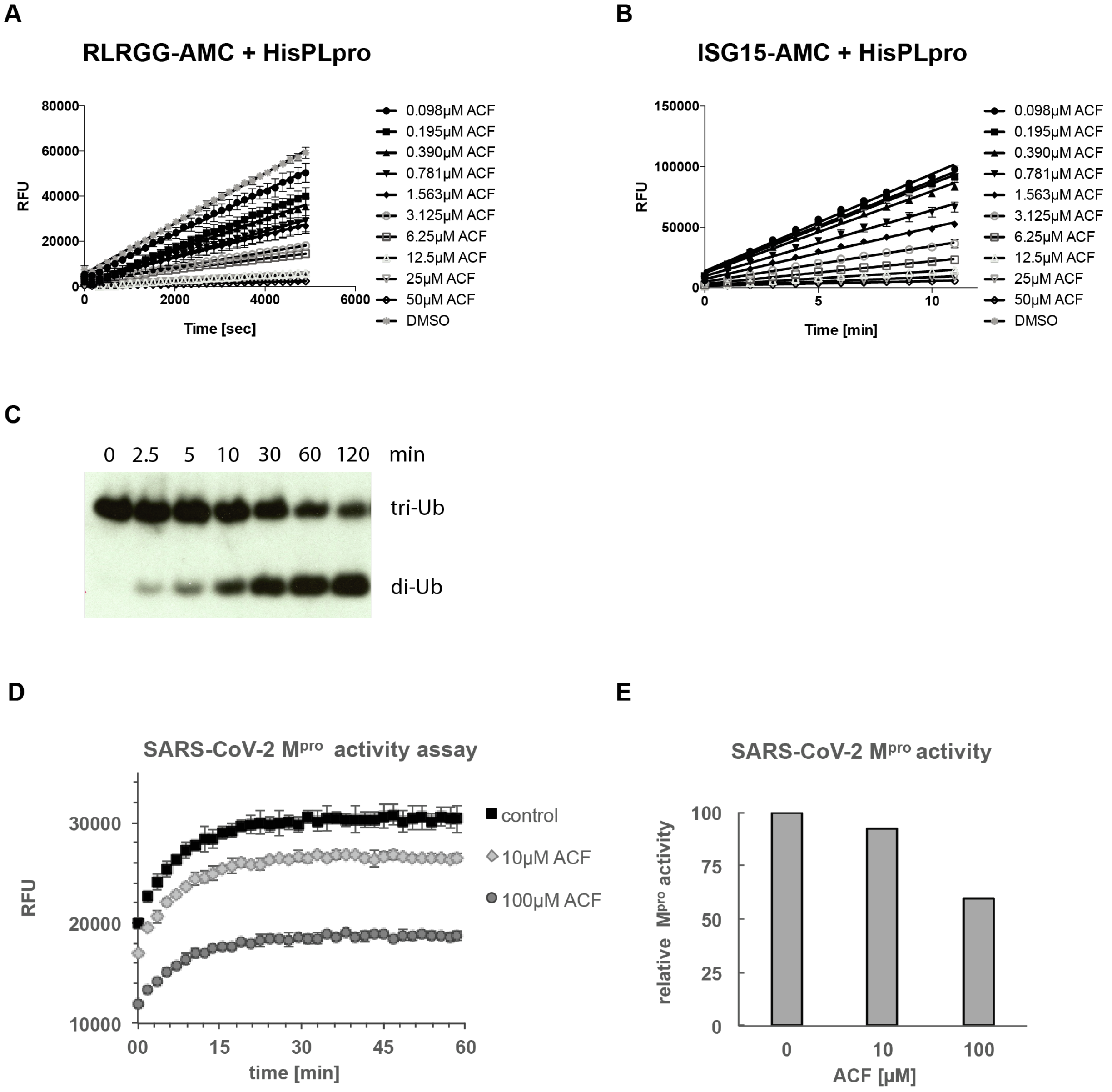

Figure S2. PL^{pro} and M^{pro} cleavage assays, Related to Figure 1 (A) and **(B)** Kinetic assays of His-PL^{pro} activity in the presence of different concentrations of ACF. RLRGG-AMC in **(A)** and ISG15-AMC in **(B)** were used as substrates. Reactions were performed in triplicates. **(C)** Time-course analysis of tri-ubiquitin K48-linked (2 µM) hydrolysis using 100 nM His-PL^{pro} **(D)** The digestion of fluorogenic substrate was recorded in the absence and presence of ACF. The vertical shift in signal levels is caused by ACF absorbance. **(E)**. Only a small decrease of M^{pro} activity is observed at a physiologically irrelevant ACF concentration of 100 µM.

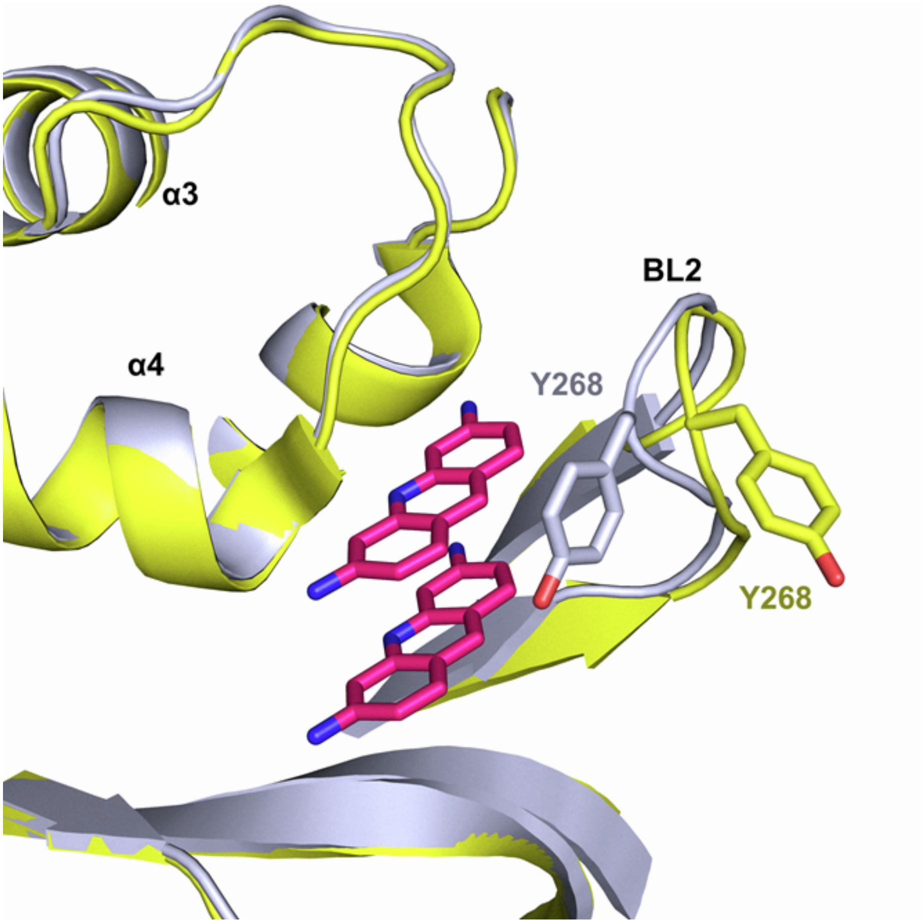

Figure S3. Comparison of SARS-CoV2-PL^{pro} in the proflavine-bound and apo-state, Related to Figure 2. Bound PL^{pro} is colored in gray; whereas the unbound PL^{pro} (PDB ID: 7D47) is colored in yellow. The BL2 loop is involved in an induced-fit rearrangement upon the binding mostly due to the movement of the Tyr268. The side-chain of Tyr268 participates in a π-π stacking with proflavine molecules.

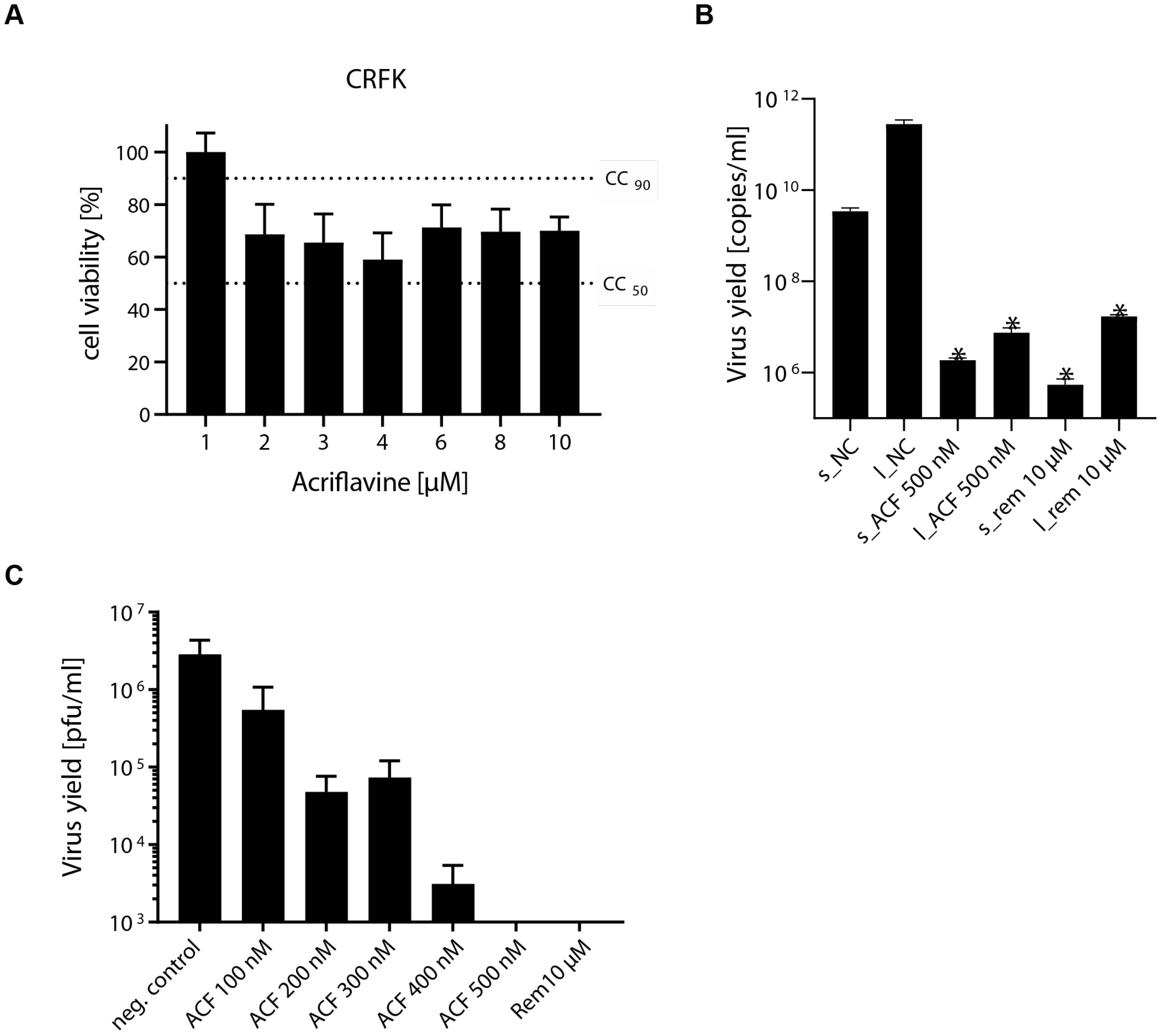

Supplementary Figure S4. Cell-based assays with ACF, Related to Figure 3. (A) The cytotoxicity of ACF in CRFK cells. **(B)** ACF Inhibits intracellular replication of SARS-CoV-2 *in vitro* in Vero cells. The figure shows RT-qPCR analysis of cell culture supernatants and lysates infected with SARS-CoV-2 at 1600 $TCID_{50}$/ml 24 h post-infection. The experiment was performed in triplicate. s_: supernatants; l_: cel lysates. NC: non-treated control, rem: remdesivir. The results are presented as average values with standard deviations (error bars). An asterisk indicates values that are significantly different from the control ($p< 0.05$). **(C)** Inhibition of virus replication by ACF in Vero cells. Inhibition of viral replication in Vero cells by ACF was evaluated with the plaque assay and is presented as change of titer.

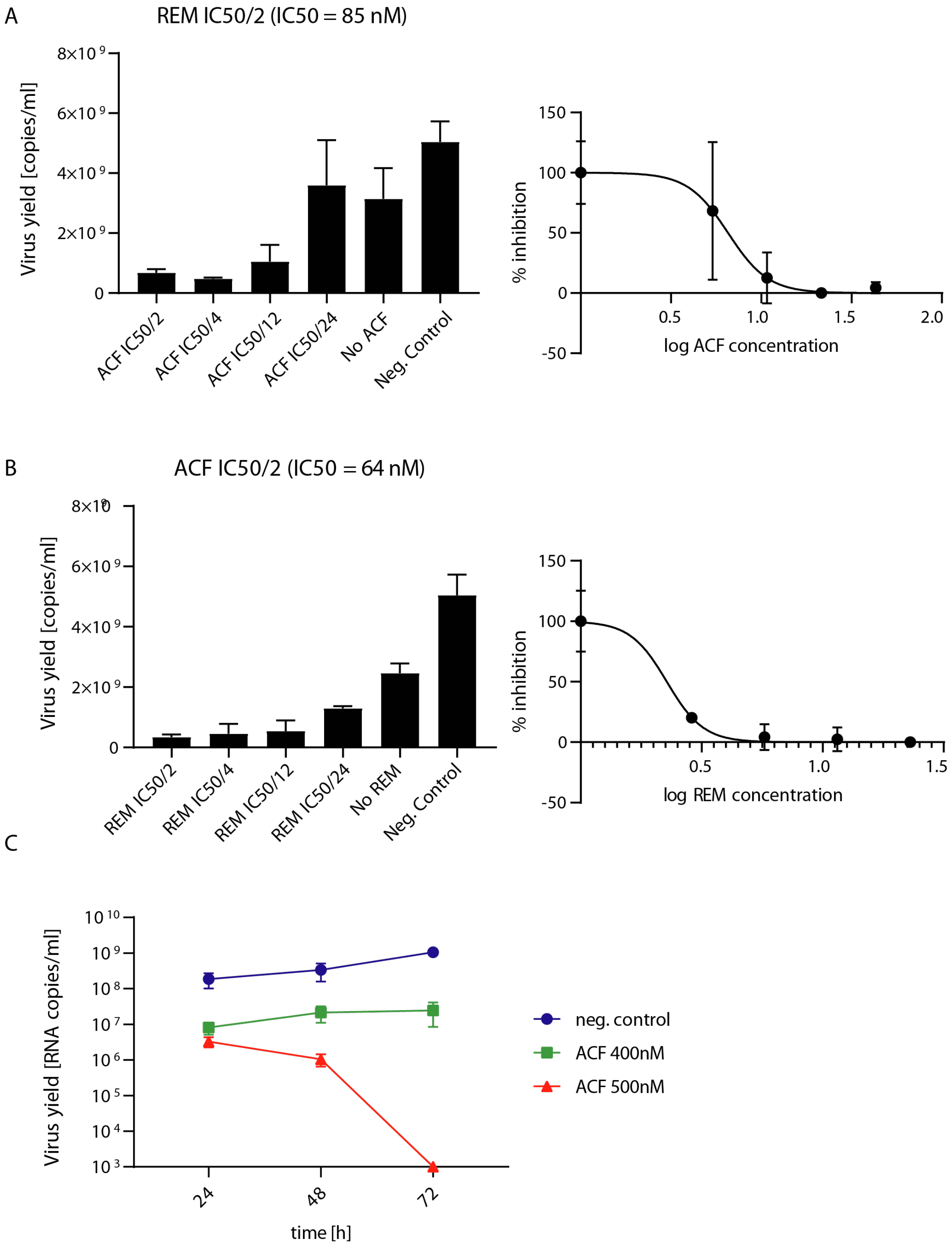

Supplementary Figure S5. Synergistic effect of ACF and remdesivir, Related to Figure 4. Inhibition of virus replication by ACF and remdesivir (REM) in Vero cells. The figure shows qRT-PCR analyses carried out 48 h post-infection of cell culture supernatants from cultures infected with SARS-CoV-2 at 1600 TCID50/ml. (**A**) Inhibition of virus with constant concentration of remdesivir with decreasing concentration of ACF. (**B**) Inhibition of virus with constant concentration of ACF with decreasing concentration of remdesivir. **(C)** ACF blocks SARS-CoV-2 replication *in vitro* and *ex vivo.* Antiviral activity of ACF against SARS-CoV-2 in human airway epithelium (prepared in-house). The figure shows RT-qPCR analysis of HAE culture supernatants infected with SARS-CoV-2. The assay was performed at least in duplicate, and median values with range are presented. Two-way ANOVA analysis with Dunnett's post-hoc test indicated that ACF and REM significantly inhibit virus yields during infection course compared to untreated control.

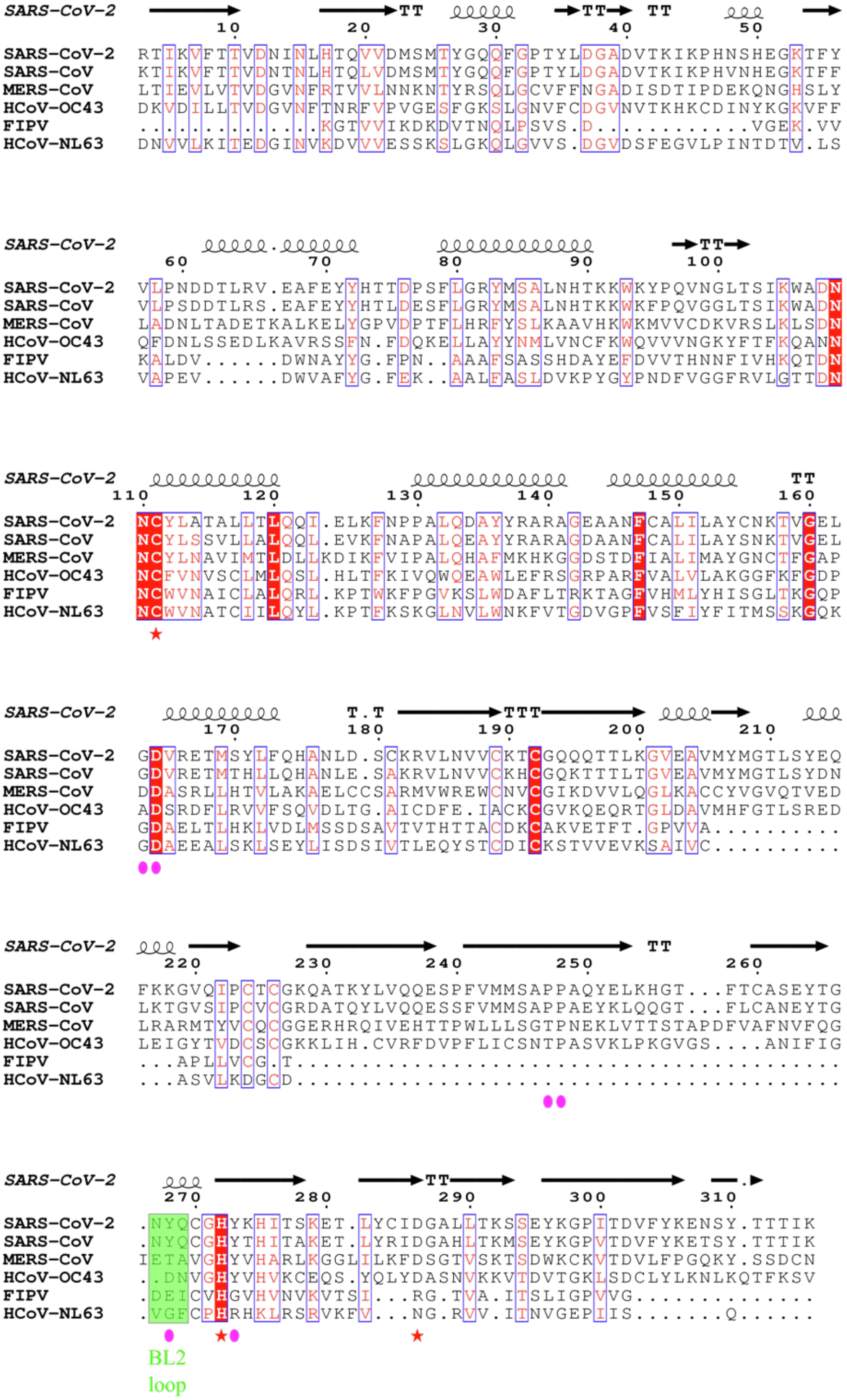

Supplementary Figure S6. Multiple sequence alignment for PL^{pro} from selected alpha- and beta-coronaviruses, Related to Figure 5. The multiple sequence alignment was generated with ESPript3 (Robert and Gouet, 2014). Residues with high SimilarityGlobalScore are highlighted as red characters on a white background or white characters on a red background (if residues are strictly conserved in the column) with blue frames. Residues from BL2 loop are marked in green. A red star indicates the catalytic residues. Purple circles indicate residues involved in the recognition of the proflavine I and proflavine II molecules. These latter vary between alpha- and beta-coronaviruses especially for concerning the amino acids contacting proflavine I, which may rationalize why ACF does not inhibit PL^{pro} from alphacoronaviruses (FIPV, HCoV-NL63).

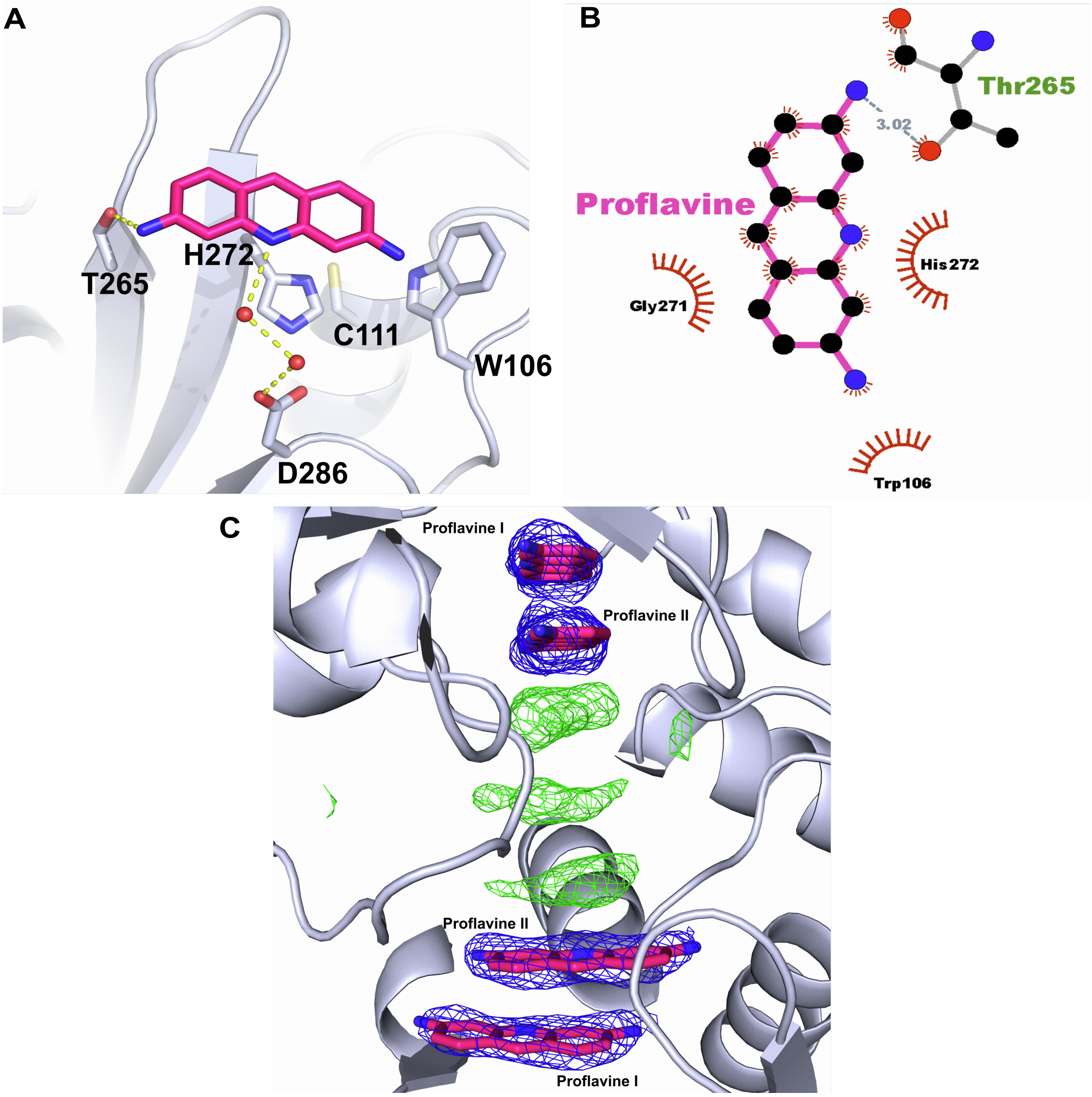

Supplementary Figure S7. Proflavine molecule at the interface between SARS-CoV2-PL^{pro} asymmetric units, Related to Figure 2. (A) Most probably due to a crystal packing molecule of proflavine was found on top of the catalytic triad (C111, H272, D286). Important residues are highlighted as stick model. Two water molecules (red spheres) mediate a hydrogen bond with D286. Hydrogen bonds are represented as yellow dashed lines. **(B)** 2D plot of the molecular interactions between proflavine and the residues of SARS-CoV-2-PL^{pro}. **(C)** Electron density map showing the fractional presence of additional aromatic proflavine-like molecules π-π stacked one on top of the other between two copies of SARS-CoV2-PL^{pro} present in the crystal lattice. $2F_o$-F_c electron density map is contoured at 2σ. The electron density of the identified proflavine molecules is colored in blue; whereas additional electron density is colored in green. The densities are most likely caused by weak and transiently-bound proflavines. We did not model them in the crystal structure as their electron density was much weaker than active site-bound molecules

SUPPLEMENTARY TABLES

Supplementary Table S1.
Compounds selected from the library for validation as PL^{pro} inhibitors, Related to Figure S1.

no	**Compound**
1	Verteporfin
2	Evans Blue
3	Clofazimine
4	Hypericin from *Hypericus perforatum*
5	Dithranol
6	Chlorophyllin sodium copper salt
7	Acriflavine hydrochloride
8	Protoporphyrin IX
9	Tannic acid
10	PHA-665752 hydrate
11	Proflavine hemisulfate salt hydrate

Supplementary Table S2.
Primers and probes used for a RT-qPCR, Related to Figure 3+4+5+7.

Target	Primer	Sequence	Concentration [nM]
SARS-CoV-2	Forward	CAC ATT GGC ACC CGC AAT C	600
	Reverse	GAG GAA CGA GAA GAG GCT TG	800
	Probe	ACT TCC TCA AGG AAC AAC ATT GCC A (FAM / BHQ1)	200
MERS-CoV	Forward	GGG TGT ACC TCT TAA TGC CAA TTC	500
	Reverse	TCT GTC CTG TCT CCG CCA AT	500
	Probe	ACC CCT GCG CAA AAT GCT GGG (FAM / TAMRA)	200
HCoV-NL63	Forward	AAA CCT CGT TGG AAG CGT GT	500
	Reverse	CTG TGG AAA ACC TTT GGC ATC	500
	Probe	TGT TAT TCA GTG CTT TGG TCC TCG TGA T (FAM / TAMRA)	100
FIPV	Forward	TCT CGT GGT CGG AAG AAT AAT G	500
	Reverse	GAA CAA GGT CTC TCG GAC ATA AA	500
	Probe	CCC ATT ACC CTC GAA CAA GGA TCT (FAM/BHQ1)	200
HCoV-OC43	Forward	AGC AAC CAG GCT GAT GTC AAT ACC	500
	Reverse	AGC AGA CCT TCC TGA GCC TTC AAT	500
	Probe	TGA CAT TGT CGA TCG GGA CCC AAG TA (FAM/BHQ1)	200

Supplementary Table S3.
Data collection and refinement statistics, Related to Figure 2.

	SCov2-PLpro-Proflavine (PDB ID:7NT4)
Data collection	
Space group	$P6_522$
Cell dimensions	
a, *b*, *c* (Å)	111.37, 116.37, 253.57
α, β, γ (°)	90, 90, 120
Resolution (Å)	49.4(2.68) *
Wavelength (Å)	1.00
R_{pim}	8.6(46.1)
$I / \sigma I$	51.9(1.8)
Completeness (%)	95.7(72.2)
Redundancy	38.1
Observed reflections	801001 (29586)
Unique reflections	21442 (1073)
Refinement	
Resolution (Å)	40 (2.68)
No. reflections	22325
R_{work} / R_{free}	19.3/ 26.4
No. atoms	
Protein	2
Ligand/ion	6
Water	193
B-factors	
Protein	43.9
Ligand/ion	61.33
Water	25.2
R.m.s. deviations	
Bond lengths (Å)	0.014
Bond angles (°)	2.16
Ramachandran statistics (%)	
Most favored regions	93.3
Additionally allowed regions	5.2
Generously allowed regions	1.5

*A single crystal was used for data collection and structure determination. *Values in parentheses are for highest-resolution shell.

Supplementary Table S4.
ACF IC_{50} values on HAE cultures at different time points, Related to Figure 4.

Time post-infecton	**IC_{50}**	**Log IC_{50}**	**Std. error (Log IC_{50})**
24 h	14.03 nM	1.147	0.83
48 h	12.59 nM	1.100	22.11
72 h	65.85 nM	1.819	1.85
96 h	61.97 nM	1.792	0.85

Supplementary Table S5.
Pharmacokinetic parameters, Related to Figure 6.

Selected pharmacokinetic parameters for ACF components in male CD-1 mice following administration of 15 and 100 mg/kg of ACF hydrochloride IV and PO respectively. ACF is a mixture of four major components; fractional doses are calculated based on composition analysis (see supplementary analysis):

	Sample	Administration/ fractional dose (mg/kg)	Pharmacokinetic Parameters		
			C_{max} (ng/mL)	$AUC_{0\rightarrow t\ min}$ (ng*min/ml)	$T_{1/2}$ (min)
Plasma	ACF	IV / 2.5	205	4870	66.2
		PO / 17	BQL	BQL	ND
	PF	IV / 8.4	1060	43800	102
		PO / 56	461	32700	ND
	Side methylated ACF	IV / 0.6	54.7	1450	61.3
		PO / 4.0	BQL	BQL	ND
	Side methylated PF	IV / 3.3	217	7720	56.1
		PO / 22	60.9	4690	ND
Lungs	ACF	IV / 2.5	7380	574000	332
		PO / 17	1960	7530	ND
	PF	IV / 8.4	43800	1650000	66.5
		PO / 56	14100	1130000	ND
	Side methylated ACF	IV / 0.6	1930	118000	185
		PO / 4.0	460	8380	178
	Side methylated PF	IV / 3.3	15400	445000	50.1
		PO / 22	3590	225000	ND

BLQ – Below the lower limit of quantitation (LLOQ)

ND – Not determined